

ZEUS Results on the Measurement and Phenomenology of F_2 at Low x and Low Q^2

Abstract

Measurements of the proton structure function F_2 for $0.6 < Q^2 < 17 \text{ GeV}^2$ and $1.2 \times 10^{-5} < x < 1.9 \times 10^{-3}$ from ZEUS 1995 shifted vertex data are presented. From ZEUS F_2 data the slopes $dF_2/d\ln Q^2$ at fixed x and $d\ln F_2/d\ln(1/x)$ for $x < 0.01$ at fixed Q^2 are derived. For the latter E665 data are also used. The transition region in Q^2 is explored using the simplest non-perturbative models and NLO QCD. The data at very low $Q^2 \leq 0.65 \text{ GeV}^2$ are described successfully by a combination of generalised vector meson dominance and Regge theory. From a NLO QCD fit to ZEUS data the gluon density in the proton is extracted in the range $3 \times 10^{-5} < x < 0.7$. Data from NMC and BCDMS constrain the fit at large x . Assuming the NLO QCD description to be valid down to $Q^2 \sim 1 \text{ GeV}^2$, it is found that the $q\bar{q}$ sea distribution is still rising at small x and the lowest Q^2 values whereas the gluon distribution is strongly suppressed.

The ZEUS Collaboration

J. Breitweg, S. Chekanov, M. Derrick, D. Krakauer, S. Magill, D. Mikunas, B. Musgrave,
J. Repond, R. Stanek, R.L. Talaga, R. Yoshida, H. Zhang

Argonne National Laboratory, Argonne, IL, USA ^p

M.C.K. Mattingly

Andrews University, Berrien Springs, MI, USA

F. Anselmo, P. Antonioli, G. Bari, M. Basile, L. Bellagamba, D. Boscherini, A. Bruni,
G. Bruni, G. Cara Romeo, G. Castellini¹, L. Cifarelli², F. Cindolo, A. Contin, N. Coppola,
M. Corradi, S. De Pasquale, P. Giusti, G. Iacobucci, G. Laurenti, G. Levi, A. Margotti,
T. Massam, R. Nania, F. Palmonari, A. Pesci, A. Polini, G. Sartorelli, Y. Zamora Garcia³,
A. Zichichi

University and INFN Bologna, Bologna, Italy ^f

C. Amelung, A. Bornheim, I. Brock, K. Coböken, J. Crittenden, R. Deffner, M. Eckert,
M. Grothe⁴, H. Hartmann, K. Heinloth, L. Heinz, E. Hilger, H.-P. Jakob, A. Kappes,
U.F. Katz, R. Kerger, E. Paul, M. Pfeiffer, H. Schnurbusch, A. Weber, H. Wieber

Physikalisches Institut der Universität Bonn, Bonn, Germany ^c

D.S. Bailey, O. Barret, W.N. Cottingham, B. Foster, R. Hall-Wilton, G.P. Heath,
H.F. Heath, J.D. McFall,

D. Piccioni, D.G. Roff, J. Scott, R.J. Tapper

H.H. Wills Physics Laboratory, University of Bristol, Bristol, U.K. ^o

M. Capua, L. Iannotti, A. Mastroberardino, M. Schioppa, G. Susinno

Calabria University, Physics Dept. and INFN, Cosenza, Italy ^f

J.Y. Kim, J.H. Lee, I.T. Lim, M.Y. Pac⁵

Chonnam National University, Kwangju, Korea ^h

A. Caldwell⁶, N. Cartiglia, Z. Jing, W. Liu, B. Mellado, J.A. Parsons, S. Ritz⁷, S. Sampson,
F. Sciulli, P.B. Straub, Q. Zhu

Columbia University, Nevis Labs., Irvington on Hudson, N.Y., USA ^q

P. Borzemski, J. Chwastowski, A. Eskreys, J. Figiel, K. Klimek, M.B. Przybycień, L. Zawiejski

Inst. of Nuclear Physics, Cracow, Poland ^j

L. Adamczyk⁸, B. Bednarek, M. Bukowy, A.M. Czermak, K. Jeleń, D. Kisielewska,
T. Kowalski,

M. Przybycień, E. Rulikowska-Zarębska, L. Suszycki, J. Zając

*Faculty of Physics and Nuclear Techniques, Academy of Mining and Metallurgy, Cracow,
Poland ^j*

Z. Duliński, A. Kotański

Jagellonian Univ., Dept. of Physics, Cracow, Poland ^k

L.A.T. Bauerdick, U. Behrens, H. Beier⁹, J.K. Bienlein, K. Desler, G. Drews, U. Fricke,
F. Goebel, P. Göttlicher, R. Graciani, T. Haas, W. Hain, G.F. Hartner, D. Hasell¹⁰,
K. Hebbel, K.F. Johnson¹¹, M. Kasemann, W. Koch, U. Kötz, H. Kowalski, L. Lindemann,
B. Löhr, M. Martínez, J. Milewski¹², M. Milite, T. Monteiro¹³, D. Notz, A. Pellegrino,
F. Pelucchi, K. Piotrkowski, M. Rohde, J. Roldán¹⁴, J.J. Ryan¹⁵, P.R.B. Saull,
A.A. Savin, U. Schneekloth, O. Schwarzer, F. Selonke, M. Sievers, S. Stonjek, B. Surrow¹³,
E. Tassi, D. Westphal¹⁶, G. Wolf, U. Wollmer, C. Youngman, W. Zeuner

Deutsches Elektronen-Synchrotron DESY, Hamburg, Germany

B.D. Burow, C. Coldewey, H.J. Grabosch, A. Meyer, S. Schlenstedt
DESY-IfH Zeuthen, Zeuthen, Germany
 G. Barbagli, E. Gallo, P. Pelfer
University and INFN, Florence, Italy ^f
 G. Maccarrone, L. Votano
INFN, Laboratori Nazionali di Frascati, Frascati, Italy ^f
 A. Bamberger, S. Eisenhardt, P. Markun, H. Raach, T. Trefzger¹⁷, S. Wöfle
Fakultät für Physik der Universität Freiburg i.Br., Freiburg i.Br., Germany ^c
 J.T. Bromley, N.H. Brook, P.J. Bussey, A.T. Doyle¹⁸, S.W. Lee, N. Macdonald, G.J. McCance, D.H. Saxon,
 L.E. Sinclair, I.O. Skillicorn, E. Strickland, R. Waugh
Dept. of Physics and Astronomy, University of Glasgow, Glasgow, U.K. ^o
 I. Bohnet, N. Gendner, U. Holm, A. Meyer-Larsen, H. Salehi, K. Wick
Hamburg University, I. Institute of Exp. Physics, Hamburg, Germany ^c
 A. Garfagnini, I. Gialas¹⁹, L.K. Gladilin²⁰, D. Kçira²¹, R. Klanner, E. Lohrmann,
 G. Poelz, F. Zetsche
Hamburg University, II. Institute of Exp. Physics, Hamburg, Germany ^c
 T.C. Bacon, I. Butterworth, J.E. Cole, G. Howell, L. Lamberti²², K.R. Long, D.B. Miller,
 N. Pavel, A. Priniyas²³, J.K. Sedgbeer, D. Sideris, R. Walker
Imperial College London, High Energy Nuclear Physics Group, London, U.K. ^o
 U. Mallik, S.M. Wang, J.T. Wu²⁴
University of Iowa, Physics and Astronomy Dept., Iowa City, USA ^p
 P. Cloth, D. Filges
Forschungszentrum Jülich, Institut für Kernphysik, Jülich, Germany
 T. Ishii, M. Kuze, I. Suzuki²⁵, K. Tokushuku²⁶, S. Yamada, K. Yamauchi, Y. Yamazaki
Institute of Particle and Nuclear Studies, KEK, Tsukuba, Japan ^g
 S.J. Hong, S.B. Lee, S.W. Nam²⁷, S.K. Park
Korea University, Seoul, Korea ^h
 H. Lim, I.H. Park, D. Son
Kyungpook National University, Taegu, Korea ^h
 F. Barreiro, J.P. Fernández, G. García, C. Glasman²⁸, J.M. Hernández²⁹, L. Hervás¹³,
 L. Labarga, J. del Peso, J. Puga, I. Redondo, J. Terrón, J.F. de Trocóniz
Univer. Autónoma Madrid, Depto de Física Teórica, Madrid, Spain ⁿ
 F. Corriveau, D.S. Hanna, J. Hartmann, W.N. Murray, A. Ochs, M. Riveline, D.G. Stairs,
 M. St-Laurent
McGill University, Dept. of Physics, Montréal, Québec, Canada ^{a, b}
 T. Tsurugai
Meiji Gakuin University, Faculty of General Education, Yokohama, Japan
 V. Bashkurov, B.A. Dolgoshein, A. Stifutkin
Moscow Engineering Physics Institute, Moscow, Russia ^l
 G.L. Bashindzhagyan, P.F. Ermolov, Yu.A. Golubkov, L.A. Khein, N.A. Korotkova,
 I.A. Korzhavina, V.A. Kuzmin, O.Yu. Lukina, A.S. Proskuryakov, L.M. Shcheglova³⁰,
 A.N. Solomin³⁰, S.A. Zotkin
Moscow State University, Institute of Nuclear Physics, Moscow, Russia ^m

C. Bokel, M. Botje, N. Brümmer, J. Engelen, E. Koffeman, P. Kooijman, A. van Sighem, H. Tiecke, N. Tuning, W. Verkerke, J. Vosseveld, L. Wiggers, E. de Wolf
*NIKHEF and University of Amsterdam, Amsterdam, Netherlands*ⁱ

D. Acosta³¹, B. Bylsma, L.S. Durkin, J. Gilmore, C.M. Ginsburg, C.L. Kim, T.Y. Ling, P. Nylander, T.A. Romanowski³²
Ohio State University, Physics Department, Columbus, Ohio, USA^p

H.E. Blaikley, R.J. Cashmore, A.M. Cooper-Sarkar, R.C.E. Devenish, J.K. Edmonds, J. Große-Knetter³³, N. Harnew, C. Nath, V.A. Noyes³⁴, A. Quadt, O. Ruske, J.R. Tickner³⁵, R. Walczak, D.S. Waters
Department of Physics, University of Oxford, Oxford, U.K.^o

A. Bertolin, R. Brugnera, R. Carlin, F. Dal Corso, U. Dosselli, S. Limentani, M. Morandin, M. Posocco, L. Stanco, R. Stroili, C. Voci
Dipartimento di Fisica dell' Università and INFN, Padova, Italy^f

B.Y. Oh, J.R. Okrasinski, W.S. Toothacker, J.J. Whitmore
Pennsylvania State University, Dept. of Physics, University Park, PA, USA^q

Y. Iga
Polytechnic University, Sagamihara, Japan^g

G. D'Agostini, G. Marini, A. Nigro, M. Raso
Dipartimento di Fisica, Univ. 'La Sapienza' and INFN, Rome, Italy^f

J.C. Hart, N.A. McCubbin, T.P. Shah
Rutherford Appleton Laboratory, Chilton, Didcot, Oxon, U.K.^o

D. Epperson, C. Heusch, J.T. Rahn, H.F.-W. Sadrozinski, A. Seiden, R. Wichmann, D.C. Williams
University of California, Santa Cruz, CA, USA^p

H. Abramowicz³⁶, G. Briskin³⁷, S. Dagan³⁸, S. Kananov³⁸, A. Levy³⁸
Raymond and Beverly Sackler Faculty of Exact Sciences, School of Physics, Tel-Aviv University, Tel-Aviv, Israel^e

T. Abe, T. Fusayasu, M. Inuzuka, K. Nagano, K. Umemori, T. Yamashita
Department of Physics, University of Tokyo, Tokyo, Japan^g

R. Hamatsu, T. Hirose, K. Homma³⁹, S. Kitamura⁴⁰, T. Matsushita, T. Nishimura
Tokyo Metropolitan University, Dept. of Physics, Tokyo, Japan^g

M. Arneodo¹⁸, R. Cirio, M. Costa, M.I. Ferrero, S. Maselli, V. Monaco, C. Peroni, M.C. Petrucci, M. Ruspa, R. Sacchi, A. Solano, A. Staiano
Università di Torino, Dipartimento di Fisica Sperimentale and INFN, Torino, Italy^f

M. Dardo
II Faculty of Sciences, Torino University and INFN - Alessandria, Italy^f

D.C. Bailey, C.-P. Fagerstroem, R. Galea, T. Koop, G.M. Levman, J.F. Martin, R.S. Orr, S. Polenz, A. Sabetfakhri, D. Simmons
University of Toronto, Dept. of Physics, Toronto, Ont., Canada^a

J.M. Butterworth, C.D. Catterall, M.E. Hayes, E.A. Heaphy, T.W. Jones, J.B. Lane, R.L. Saunders, M.R. Sutton, M. Wing
University College London, Physics and Astronomy Dept., London, U.K.^o

J. Ciborowski, G. Grzelak⁴¹, R.J. Nowak, J.M. Pawlak, R. Pawlak, B. Smalska, T. Tymieniecka,

A.K. Wróblewski, J.A. Zakrzewski, A.F. Żarnecki

Warsaw University, Institute of Experimental Physics, Warsaw, Poland^j

M. Adamus

Institute for Nuclear Studies, Warsaw, Poland^j

O. Deppe, Y. Eisenberg³⁸, D. Hochman, U. Karshon³⁸

Weizmann Institute, Department of Particle Physics, Rehovot, Israel^d

W.F. Badgett, D. Chapin, R. Cross, C. Foudas, S. Mattingly, D.D. Reeder, W.H. Smith,

A. Vaiciulis, T. Wildschek, M. Wodarczyk

University of Wisconsin, Dept. of Physics, Madison, WI, USA^p

A. Deshpande, S. Dhawan, V.W. Hughes

Yale University, Department of Physics, New Haven, CT, USA^p

S. Bhadra, W.R. Frisken, M. Khakzad, W.B. Schmidke

York University, Dept. of Physics, North York, Ont., Canada^a

¹ also at IROE Florence, Italy
² now at Univ. of Salerno and INFN Napoli, Italy
³ supported by Worldlab, Lausanne, Switzerland
⁴ now at University of California, Santa Cruz, USA
⁵ now at Dongshin University, Naju, Korea
⁶ also at DESY
⁷ Alfred P. Sloan Foundation Fellow
⁸ supported by the Polish State Committee for Scientific Research, grant No. 2P03B14912
⁹ now at Innosoft, Munich, Germany
¹⁰ now at Massachusetts Institute of Technology, Cambridge, MA, USA
¹¹ visitor from Florida State University
¹² now at ATM, Warsaw, Poland
¹³ now at CERN
¹⁴ now at IFIC, Valencia, Spain
¹⁵ now a self-employed consultant
¹⁶ now at Bayer A.G., Leverkusen, Germany
¹⁷ now at ATLAS Collaboration, Univ. of Munich
¹⁸ also at DESY and Alexander von Humboldt Fellow at University of Hamburg
¹⁹ visitor of Univ. of Crete, Greece, partially supported by DAAD, Bonn - Kz. A/98/16764
²⁰ on leave from MSU, supported by the GIF, contract I-0444-176.07/95
²¹ supported by DAAD, Bonn - Kz. A/98/12712
²² supported by an EC fellowship
²³ PPARC Post-doctoral fellow
²⁴ now at Applied Materials Inc., Santa Clara
²⁵ now at Osaka Univ., Osaka, Japan
²⁶ also at University of Tokyo
²⁷ now at Wayne State University, Detroit
²⁸ supported by an EC fellowship number ERBFMBICT 972523
²⁹ now at HERA-B/DESY supported by an EC fellowship No.ERBFMBICT 982981
³⁰ partially supported by the Foundation for German-Russian Collaboration DFG-RFBR
(grant no. 436 RUS 113/248/3 and no. 436 RUS 113/248/2)
³¹ now at University of Florida, Gainesville, FL, USA
³² now at Department of Energy, Washington
³³ supported by the Feodor Lynen Program of the Alexander von Humboldt foundation
³⁴ Glasstone Fellow
³⁵ now at CSIRO, Lucas Heights, Sydney, Australia
³⁶ an Alexander von Humboldt Fellow at University of Hamburg
³⁷ now at Brown University, Providence, RI, USA
³⁸ supported by a MINERVA Fellowship
³⁹ now at ICEPP, Univ. of Tokyo, Tokyo, Japan
⁴⁰ present address: Tokyo Metropolitan University of Health Sciences, Tokyo 116-8551,
Japan
⁴¹ supported by the Polish State Committee for Scientific Research, grant No. 2P03B09308

- a* supported by the Natural Sciences and Engineering Research Council of Canada (NSERC)
- b* supported by the FCAR of Québec, Canada
- c* supported by the German Federal Ministry for Education and Science, Research and Technology (BMBF), under contract numbers 057BN19P, 057FR19P, 057HH19P, 057HH29P
- d* supported by the MINERVA Gesellschaft für Forschung GmbH, the German Israeli Foundation, the U.S.-Israel Binational Science Foundation, and by the Israel Ministry of Science
- e* supported by the German-Israeli Foundation, the Israel Science Foundation, the U.S.-Israel Binational Science Foundation, and by the Israel Ministry of Science
- f* supported by the Italian National Institute for Nuclear Physics (INFN)
- g* supported by the Japanese Ministry of Education, Science and Culture (the Monbusho) and its grants for Scientific Research
- h* supported by the Korean Ministry of Education and Korea Science and Engineering Foundation
- i* supported by the Netherlands Foundation for Research on Matter (FOM)
- j* supported by the Polish State Committee for Scientific Research, grant No. 115/E-343/SPUB/P03/002/97, 2P03B10512, 2P03B10612, 2P03B14212, 2P03B10412
- k* supported by the Polish State Committee for Scientific Research (grant No. 2P03B08614) and Foundation for Polish-German Collaboration
- l* partially supported by the German Federal Ministry for Education and Science, Research and Technology (BMBF)
- m* supported by the Fund for Fundamental Research of Russian Ministry for Science and Education and by the German Federal Ministry for Education and Science, Research and Technology (BMBF)
- n* supported by the Spanish Ministry of Education and Science through funds provided by CICYT
- o* supported by the Particle Physics and Astronomy Research Council
- p* supported by the US Department of Energy
- q* supported by the US National Science Foundation

1 Introduction

The rapid rise of the proton structure function F_2 at low x , measured at HERA [1], continues to generate a lot of interest. In particular the persistence of the strong rise to small values of Q^2 and the apparent success of the perturbative QCD (pQCD) description of the data down to Q^2 values approaching 1 GeV^2 raise new challenges for our understanding of QCD. HERA also allows study of the ‘transition region’ as $Q^2 \rightarrow 0$ in which pQCD must break down. The theoretical context for our study of pQCD and the transition region is outlined in Sec. 2.

With data taken during the 1995 HERA run the ZEUS experiment has achieved a significant increase in the kinematic coverage for low x and low Q^2 inelastic neutral current positron-proton scattering. The coverage for Q^2 between 0.11 and 0.65 GeV^2 was made possible with the installation of a small electromagnetic sampling calorimeter, the Beam Pipe Calorimeter (BPC), at small positron scattering angles and results on the proton structure function F_2 and the total γ^*p cross-section have been published [2]. In Sec. 3 of this paper we report on further measurements of F_2 in the Q^2 range between 0.6 and 17 GeV^2 . The data were obtained from runs in which the interaction point was shifted away from the main rear calorimeter thus extending its small-angle coverage for scattered positrons. These data fill the gap in Q^2 between the BPC and the 1994 ZEUS measurements [3, 4]. Taking all three data sets together, the ZEUS experiment has measured F_2 over the kinematic region $0.1 < Q^2 < 5000 \text{ GeV}^2$, $2 \times 10^{-6} < x < 0.5$. The coverage of the kinematic plane by the ZEUS data sets is shown in Fig. 1.

The very low Q^2 data are discussed in Sec. 4 using generalised vector dominance and Regge theory and it is established that the ZEUS data with $Q^2 \leq 0.65 \text{ GeV}^2$ are well described by such approaches. In Sec. 5 the slopes $dF_2/d\ln Q^2$ at fixed x and $d\ln F_2/d\ln(1/x)$ at fixed Q^2 are derived from the combined ZEUS data sets. In Sec. 6 the ZEUS F_2 data, together with fixed target data at large x , are fit using next to leading order (NLO) QCD to determine the gluon momentum density. The increased range and precision of the ZEUS F_2 data allow a more precise extraction of the gluon density at low x compared to our earlier results using the 1993 ZEUS data [5]. In Sec. 7 the properties of the pQCD description of the F_2 and slopes data at low Q^2 are explored in more detail. Our conclusions are summarised in Sec. 8. Tables containing F_2 values and other data are given in the Appendix.

2 Phenomenology of the low Q^2 region

We use NLO pQCD and the simplest non-perturbative models to explore the transition region in Q^2 . The standard NLO DGLAP equations [6] give the Q^2 evolution of parton densities, but do not prescribe their functional form in x at the starting scale Q_0^2 . At Q_0^2 , the small x behaviour of parton momentum densities $xf(x)$ may be characterised by the exponent δ where $xf(x) \approx Ax^\delta$. For $\delta \geq 0$ a parton momentum density either tends to zero or is constant as $x \rightarrow 0$ (non-singular) while for $\delta < 0$ a parton density increases as $x \rightarrow 0$ (singular). One way to understand the rise of F_2 at low x is advocated by Glück, Reya and Vogt (GRV) [7, 8] who argue that the starting scale for the evolution of the parton densities should be very low (0.34 GeV^2) and at the starting scale the

¹Bjorken x and the negative squared momentum transfer, Q^2 , are defined in Sec. 3.2.

parton density functions should be non-singular. For $Q^2 > 1 \text{ GeV}^2$, the observed rise in F_2 is then generated dynamically through the DGLAP evolution equations. On the other hand, at low x one might expect that the DGLAP equations break down because of large $\ln(1/x)$ terms that are not included. Such terms are taken into account by the BFKL formalism [9], which in leading order predicts a rising F_2 at low x . The rise comes from a singular gluon density with δ in the range -0.3 to -0.5 . Recent work on BFKL at NLO has shown that the corrections to the LO value for δ are large [10] and reduce the predicted rise in F_2 , though quite how large the reduction should be is still under discussion [11]. Clearly accurate experimental results on F_2 and δ at low x are of great interest. More details on the many alternative pQCD approaches to the low x region may be found in [12, 13].

As Q^2 decreases α_S increases and pQCD will eventually break down. Then non-perturbative models must be used to describe the data. At low x the lifetime of the virtual photon in the proton rest frame is large compared to the γ^*p interaction time [14]. Inelastic $e^\pm p$ scattering may then be viewed as γ^*p scattering, with the total γ^*p cross-section given by ²

$$\sigma_{\text{tot}}^{\gamma^*p}(W^2, Q^2) \equiv \sigma_T + \sigma_L \approx \frac{4\pi^2\alpha}{Q^2} F_2(x, Q^2), \quad (1)$$

where $W \approx \sqrt{Q^2/x}$ is the centre-of-mass energy of the γ^*p system and σ_T and σ_L are the cross-sections for transversely and longitudinally polarised virtual photons respectively. We consider two non-perturbative approaches, the vector meson dominance model (VMD) and Regge theory.

VMD relates the hadronic interactions of the photon to a sum over interactions of the ρ^0, ω and ϕ vector meson states [15, 16]. To accommodate deep inelastic scattering data the sum has to be extended to an infinite number of vector mesons giving the generalised vector dominance model (GVMD) [17]. Following the assumptions in [17], $\sigma_T(W^2, Q^2)$ is related to $\sigma^{\gamma p}(W^2)$, the total photoproduction cross-section by

$$\sigma_T(W^2, Q^2) = \left[\frac{r_C M_0^2}{(M_0^2 + Q^2)} + \sum_{V=\rho^0, \omega, \phi} \frac{r_V M_V^4}{(M_V^2 + Q^2)^2} \right] \sigma^{\gamma p}(W^2), \quad (2)$$

where M_0 is the lower cutoff of the continuum vector states and r_C, r_V are constants satisfying the normalisation condition $r_C + \sum_V r_V = 1$ at $Q^2 = 0$. A similar expression to Eq. (2) may be written for $\sigma_L(W^2, Q^2)$, but with additional Q^2 dependence to ensure that it vanishes as $Q^2 \rightarrow 0$ [17]. The GVMD approach has recently been revived in the context of low Q^2 HERA data by Schildknecht and Spiesberger [18]. We use a simplified form of GVMD to study the consistency of the data in the ZEUS BPC region and its extrapolation to $Q^2 = 0$.

Regge theory [19, 20] provides a framework in which the energy dependence of hadronic total cross-sections is of the form $\sigma \sim \sum_r \beta_r s^{\alpha_r - 1}$ where \sqrt{s} is the centre-of-mass energy, α_r the intercept of the Regge trajectory and β_r a process dependent constant. The α_r are universal and can in principle be determined from the spectrum of meson states. However, for the dominant trajectory describing total cross-sections at high energies

² Considering virtual photon exchange only. Since we are working at small x , terms depending on $M_N^2 x^2$ have been ignored.

(known as the Pomeron), this has not yet been possible. The Pomeron intercept, α_P , is determined by fitting high energy total cross-section data. Donnachie and Landshoff (DL) [21] have used a two component Pomeron+Reggeon approach to give a good description of hadron-hadron and photoproduction total cross-section data over a wide range of energies with α_P of about 1.08. They have extended their approach to γ^*p total cross-sections [22] by keeping the Regge intercept independent of Q^2 but assuming a simple Q^2 dependence for the coupling term, which becomes $\beta_r m_r^2 / (m_r^2 + Q^2)$ where m_r^2 is again determined by fitting to data.

Neither the non-perturbative VMD and DL approaches nor pQCD can be expected to describe the Q^2 behaviour of F_2 over the complete range from photoproduction to very large Q^2 deep inelastic scattering (DIS). Many models combining various aspects of these approaches have been applied to the data in the transition region [13, 23, 24]. A comparison of the ZEUS BPC data with some of the models was given in [2]. We use the DL Regge model [22] and the 1994 parton densities (GRV94) of the GRV group [8] as ‘benchmarks’ in this paper as they were available before the recent precision measurements were made.

3 Measurement of F_2 with shifted vertex data

The shifted vertex data correspond to an integrated luminosity of 236 nb^{-1} taken in a special running period in which the nominal interaction point was offset in the proton beam direction by +70 cm,³ i.e. away from the main rear calorimeter (RCAL). The measurement follows previous analyses described in more detail in [3, 4]. However, compared to the earlier shifted vertex analysis [3], for the 1995 data taking period the RCAL modules above and below the beam were moved closer to the beam, thus extending the shifted vertex Q^2 range down to 0.6 GeV^2 . The basic detector components used are the compensating uranium calorimeter (CAL), which has an energy resolution, as measured in the test beam, of $\sigma/E = 18\%/\sqrt{E(\text{GeV})}$ for electromagnetic particles and $\sigma/E = 35\%/\sqrt{E(\text{GeV})}$ for hadronic particles. The tracking chamber system is used to determine the position of the event vertex. The small angle rear tracking detector (SRTD) consists of horizontal and vertical scintillator strips covering the region around the RCAL beam hole, i.e. the region of positron scattering angles of low Q^2 events. It is also used as a preshower detector for the RCAL and has a position resolution of 0.3 cm. The luminosity is determined from the positron-proton bremsstrahlung $ep \rightarrow ep\gamma$ where the radiated photon is measured in a lead-scintillator calorimeter (LUMI) positioned at $Z = -107 \text{ m}$. There is an associated electron calorimeter (LUMI-E), positioned at $Z = -35 \text{ m}$, which is used for tagging photoproduction events. The uncertainty in the luminosity measurement is 1%.

3.1 Monte Carlo simulation

Monte Carlo (MC) events are used to correct for the detector acceptance, resolution and the effect of initial state radiation. In the framework of DJANGO [25] the generator HERACLES [26] is used to simulate neutral current DIS events including first order

³The ZEUS coordinate system is defined as right handed with the Z axis pointing in the proton beam direction, and the X axis horizontal, pointing towards the centre of HERA. The origin is at the unshifted interaction point.

electroweak radiative effects. The hadronic final state is simulated using the ARIADNE [27] program which implements the colour-dipole model. A parameterisation of the F_2 structure functions based on the results published in [4] is used and F_L is set to zero. The MC event sample is 1.6 times that of the data and the events are passed through the same offline reconstruction software as the data. Simulated photoproduction background events are generated using the program PYTHIA [28] with a cross-section given by the ALLM [29] parameterisation.

3.2 Kinematic reconstruction

The reaction $e^+(k) + p(P) \rightarrow e^+(k') + X$ at fixed squared centre-of-mass energy, $s = (k + P)^2$, is described in terms of $Q^2 \equiv -q^2 = -(k - k')^2$ and Bjorken $x = Q^2/(2P \cdot q)$. At HERA $s \approx 4E_e E_p$, where $E_e = 27.5$ GeV and $E_p = 820$ GeV denote the positron and proton beam energies. The fractional energy transferred to the proton in its rest frame is $y = Q^2/(sx)$.

The kinematic variables are reconstructed from the measured energy, E'_e , and scattering angle, θ_e , of the positron (the ‘electron method’),

$$Q^2 = 2E_e E'_e (1 + \cos \theta_e) \quad \text{and} \quad y = 1 - \frac{E'_e}{2E_e} (1 - \cos \theta_e).$$

This method gives the best resolution in the region of interest at high y and low Q^2 . Scattered positrons are identified by a neural network based algorithm [4], with an efficiency of about 90% at positron energies of 10 GeV, increasing to 100% at 20 GeV. The measured energy is corrected for energy loss in inactive material in front of the CAL using the signals in the SRTD scintillators. The uncertainty in the measured energy is estimated to be 2% at 10 GeV decreasing to 1% at 27.5 GeV. The positron impact position on the CAL measured with the SRTD together with the event vertex position measured with tracks in the CTD gives the positron scattering angle θ_e . For events outside the fiducial volume of the SRTD, the CAL position determination is used. For events in which the event vertex cannot be reconstructed, the vertex is set to the mean value of the vertex distribution.

The variable $y_{\text{JB}} = \sum_i E_i (1 - \cos \theta_i) / (2E_e)$, where the sum runs over all CAL cells except those belonging to the scattered positron, gives a measurement of y with a good resolution at low y . A cut $y_{\text{JB}} > 0.04$ is imposed to limit event migrations from low y , where the resolution of the electron method is poor, into the bins at higher y .

3.3 Event selection

Data are selected online by a three level trigger system. At the first level a certain energy deposit in the CAL is required and cuts on the arrival times of particles measured in the SRTD are imposed. At the second level the condition $\delta \equiv \sum_i E_i (1 - \cos \theta_i) > 29 \text{ GeV} - 2E_\gamma$ has to be fulfilled, where the sum goes over all CAL cells with energies E_i and polar angles θ_i , and E_γ is the energy measured in the LUMI detector. This cut significantly reduces the photoproduction background as $\delta = 2E_e$ (55 GeV) for a fully contained DIS event. At the third level a full event reconstruction is performed. A reconstructed positron with an energy greater than 4 GeV and a CAL impact point outside a box of $24(X) \text{ cm} \times 12(Y) \text{ cm}$ centered on the RCAL beam hole is required.

Also, δ has to be greater than 30 GeV and event times measured in the CAL are required to be consistent with an e^+p interaction at the nominal shifted interaction point.

The offline event selection cuts are:

- Positron finding as described above, including the requirements on the impact point and on $y_{\text{JB}} > 0.04$, with a corrected positron energy $E'_e > 10$ GeV. This ensures a high efficiency for positron finding and removes events at very high y , which suffer from large photoproduction backgrounds.
- The positron impact point on the CAL is required to be outside a box of 26 cm \times 16 cm around the RCAL beam pipe hole to ensure full shower containment in the CAL.
- 35 GeV $< \delta < 65$ GeV, in order to further reduce photoproduction and beam-gas related backgrounds. This cut also removes events with hard initial state radiation.
- For events with a tracking vertex, the reconstructed Z coordinate of the vertex is required to lie within 40 cm $< Z_{\text{vertex}} < 160$ cm. The acceptance is extended to large Z values to accommodate events from satellite bunches, i.e. proton bunches that are shifted by 4.8 ns with respect to the primary bunch crossing time, resulting in a fraction of ep interactions occurring displaced by an additional 72 cm.

A total of 62000 events pass the cuts.

3.4 Background estimation

The background from beam-gas interactions is about 1% as determined from unpaired positron and proton bunches.

The main background comes from photoproduction events, where the positron escapes along the beam line and a mis-identified positron (mainly electromagnetic showers from π^0 decays) is reconstructed in the CAL. The amount of this background is determined using the MC simulated photoproduction event sample. In total it is a small effect which is only significant at small values of E'_e and Q^2 as shown in plots (d) and (e) of Fig. 2. In a small fraction of real photoproduction events the positron is detected inside the limited acceptance of the LUMI-E electron tagger. These events are used to cross check the MC background estimate. Both results agree within 20%.

3.5 Determination of F_2

In the Q^2 range of this analysis the double differential cross-section for single virtual-photon exchange in DIS is given by

$$\frac{d^2\sigma}{dx dQ^2} = \frac{2\pi\alpha^2}{xQ^4} \left[2(1-y) + \frac{y^2}{1+R} \right] F_2(x, Q^2) \left[1 + \delta_r(x, Q^2) \right], \quad (3)$$

where R is related to the longitudinal structure function F_L by $R = F_L/(F_2 - F_L)$ and δ_r gives the radiative correction to the Born cross-section. For the kinematic range of this analysis δ_r is at most 10%. For R we take values given by the BKS model [30]. An iterative procedure is used to extract the structure function F_2 . Data and MC events are binned in the variables y and Q^2 . In a bin-by-bin unfolding procedure the MC

differential cross-section is adjusted to describe the data using a smooth function for F_2 . The re-weighted MC events are then used to unfold F_2 again, until after 3 iterations the changes to F_2 are below 0.5%. The statistical errors of the F_2 values are calculated from the number of events measured in a bin and the statistical error on the acceptance calculation from the MC simulation.

The quality of the description of the data by the re-weighted MC is shown in Fig. 2, which displays distributions of the following quantities: (a) δ or $E - P_Z$ as defined in Sec. 3.3; (b) the Z -position of the primary vertex; (c) the positron scattering angle θ_e ; (d) the energy, E'_e , of the scattered positron; (e) $\log_{10} Q^2$; (f) $\log_{10} y$. The agreement between data (filled circles) and simulated data (open histograms, normalised to the luminosity of the data) is generally good.

3.6 Systematic uncertainties

The systematic uncertainties of the measured F_2 values are determined by changing the selection cuts or the analysis procedure in turn and repeating the extraction of F_2 . Positive and negative differences, ΔF_2 , are added in quadrature separately to obtain the total positive and negative systematic errors. The systematic checks and errors are:

- A shift of the horizontal and vertical position of the SRTD by ± 0.5 mm results in $\Delta F_2/F_2$ of at most $\approx 2\%$.
- The two halves of the SRTD are moved with respect to each other in the horizontal and vertical directions by 1.0 mm, which results in $\Delta F_2/F_2$ of $\approx 4\%$.
- The uncertainty in the positron energy calibration is estimated to be 2% at 10 GeV decreasing to 1% at 27.5 GeV giving a maximum $\Delta F_2/F_2$ of 8%.
- The hadron energy scale is uncertain to $\pm 3\%$, causing a maximum $\Delta F_2/F_2$ of 2%.
- The uncertainty in the positron finder efficiency is estimated to be 2.5% at 10 GeV decreasing to 1% at 27.5 GeV, which gives $\Delta F_2/F_2$ of at most 2%.
- The number of MC events in satellite bunches is increased by 100% and decreased to 50%. This leads to a $\Delta F_2/F_2$ less than 2%.
- The uncertainty in the determination of the photoproduction background by MC is estimated to be 30%. The resulting maximum $\Delta F_2/F_2$ is about 7% in the highest y bins.
- The vertex finding efficiency is between 75% and 95% depending on the kinematic region. To study the effect of differences in the efficiency between MC and data all vertices are assigned to the nominal interaction point. $\Delta F_2/F_2$ is at most 6%.
- A variation in the box cut from 26 cm \times 16 cm to 25.6 cm \times 15.6 cm or 26.4 cm \times 8.4 cm, giving a maximum change $\Delta F_2/F_2$ of 7%.

The acceptance for DIS events with a rapidity gap at low Q^2 is somewhat different from that of non-diffractive events due to the different energy flow. To check the effect on F_2 , the acceptance for diffractive events is first calculated using a separate diffractive MC.⁴

⁴A modification of the ARIADNE MC adjusted to generate rapidity gap events as described in [4].

Using this and the measured fraction of rapidity gap events in each bin, the acceptance function is recalculated. The largest change to F_2 is 2.5%. The data are corrected for this effect. Half the correction value is taken as the estimate of the systematic error, reflecting mainly the uncertainty in the fraction of diffractive events.

In addition there is an overall normalisation uncertainty of 1.5%, due to the 1% error in the luminosity measurement and a 1% uncertainty in the trigger efficiency, which is not included in the point to point systematic error estimate.

The F_2 data cover the x range $1.2 \times 10^{-5} - 1.9 \times 10^{-3}$ in 12 bins of Q^2 between 0.6 and 17 GeV² (ZEUS SVX95). The values for F_2 and their systematic errors are given in Table 1 of the Appendix. Fig. 3 shows the results for F_2 as a function of x in the 12 Q^2 bins. In the lowest Q^2 bin data from ZEUS F_2 measurements at very low Q^2 using the BPC (BPC95) [2] are shown and at larger Q^2 those from the ZEUS94 measurements [4]. Also shown are data from the shifted vertex measurements by H1 (H1 SVX95) [31] and fixed target data from E665 [32]. There is good agreement between the different ZEUS data sets and between ZEUS, E665 and H1 data in the regions of overlap. We note that the steep increase of F_2 at low x observed in the higher Q^2 bins softens at the lowest Q^2 values. The curves shown will be discussed later.

4 The low Q^2 region

We first give an overview of the $Q^2 \leq 4.55$ GeV² region. Fig. 4 shows the ZEUS cross-section data versus W^2 derived from the SVX95, BPC95 and ZEUS94 F_2 values using Eq. (1). Also shown are data from H1 SVX95 and measurements of the total cross-section for scattering of real photons on protons at fixed target [33] and HERA energies [34]. The two curves shown are the predictions of the DL Regge model [22] and $\sigma_{\text{tot}}^{\gamma^*p}$ calculated from the NLO QCD parton distributions of GRV94 [8]. The DL model predicts that the cross-section rises slowly with energy $\propto W^{2\lambda}$, $\lambda = 1 - \alpha_P \approx 0.08$ and this behaviour seems to be followed by the data at very low Q^2 values, although the normalisation of the DL model is low compared to the ZEUS BPC95 data. Above $Q^2 = 0.65$ GeV², the DL model predicts a shallower rise of the cross-section than the data exhibit. For Q^2 values around 1 GeV² and above, the GRV94 curves describe the qualitative behaviour of the data, namely the increasing rise of $\sigma_{\text{tot}}^{\gamma^*p}$ with W^2 , as Q^2 increases. This suggests that the pQCD calculations can account for a significant fraction of the cross-section at the larger Q^2 values.

For the remainder of this section we concentrate on non-perturbative descriptions of the ZEUS BPC95 data ($0.11 < Q^2 < 0.65$ GeV²). Since the BPC data are binned in Q^2 and y we first rewrite the double differential cross-section of Eq. (3) (dropping the radiative correction factor) as

$$\frac{d^2\sigma}{dydQ^2} = \Gamma \cdot (\sigma_T + \epsilon\sigma_L) \quad (4)$$

where $\sigma_L = \frac{Q^2}{4\pi^2\alpha} F_L$ and $\sigma_T + \sigma_L$ has been defined by Eq. (1). The virtual photons have flux $\Gamma = \alpha(1 + (1 - y)^2)/(2\pi Q^2 y)$ and polarisation $\epsilon = 2(1 - y)/(1 + (1 - y)^2)$. For the BPC data ϵ lies in the range 0.55 – 0.99 but as s is fixed at HERA, ϵ cannot be varied independently of x and Q^2 . Thus the experimentally determined quantity is the combination $\sigma_T + \epsilon\sigma_L$. For simplicity we keep only the continuum term in the GVMD

expression of Eq. (2). At a fixed W the longitudinal and transverse γ^*p cross-sections are then related to the corresponding cross-section $\sigma_0^{\gamma p}$ at $Q^2 = 0$ by

$$\begin{aligned}\sigma_L(W^2, Q^2) &= \xi \left[\frac{M_0^2}{Q^2} \ln \frac{M_0^2 + Q^2}{M_0^2} - \frac{M_0^2}{M_0^2 + Q^2} \right] \sigma_0^{\gamma p}(W^2) \\ \sigma_T(W^2, Q^2) &= \frac{M_0^2}{M_0^2 + Q^2} \sigma_0^{\gamma p}(W^2),\end{aligned}\tag{5}$$

where the parameter ξ is the ratio $\sigma_L^{Vp}/\sigma_T^{Vp}$ for vector meson (V) proton scattering and M_0 is the effective vector meson mass. Neither ξ nor M_0 are given by the model and they are usually determined from data. We set σ_L to zero because ξ is expected to be less than one⁵ and the factor in the square bracket in the expression for σ_L is small (for $Q^2 \leq 0.65 \text{ GeV}^2$ and $M_0 \approx m_\rho$, it is less than 0.2). The Q^2 dependence of the BPC data, in 8 bins of W between 104 and 251 GeV, is fit with a single mass parameter M_0^2 . The cross-sections, $\sigma_0^{\gamma p}(W^2)$, are also fit at each W giving a total of 9 parameters. The fit is reasonable ($\chi^2/ndf = 38.7/(34 - 9) = 1.55$, statistical errors only) as shown in the upper plot of Fig. 5. To estimate the systematic errors, the fit is first repeated for each systematic check on the BPC data, using data and statistical errors corresponding to that change. The systematic errors are then determined by adding in quadrature the changes from the nominal values of the parameters. As a final check on the stability of the results, the fit is repeated including the longitudinal term with $\xi = 0.4$. The resulting changes in the values for the cross-sections are less than their statistical errors (more details are given in [36]). The value obtained for M_0^2 is $0.53 \pm 0.04(\text{stat}) \pm 0.09(\text{sys}) \text{ GeV}^2$. The resulting extrapolated values of $\sigma_0^{\gamma p}$ are given in Table 2 of the Appendix and shown as a function of W^2 in the lower plot of Fig. 5, along with measurements from HERA and lower energy experiments. The BPC $\sigma_0^{\gamma p}$ values lie somewhat above the direct measurements from HERA. They are also above the prediction of Donnachie and Landshoff. It should be clearly understood that the $\sigma_0^{\gamma p}$ values derived from the BPC are not a measurement of the total photoproduction cross-section but the result of a phenomenologically motivated extrapolation.

The simple GVMD approach just described gives a concise account of the Q^2 dependence of the BPC data. To describe the energy dependence of the data we use a two component Regge model

$$\sigma_{\text{tot}}^{\gamma p}(W^2) = A_R(W^2)^{\alpha_R-1} + A_P(W^2)^{\alpha_P-1}$$

where P and R denote the Pomeron and Reggeon contributions. The Reggeon intercept α_R is fixed to the value 0.5 which is compatible with the original DL value [21], and recent estimates [37, 38]. Fitting only the Pomeron term to the extrapolated BPC data ($\sigma_0^{\gamma p}$) gives $\alpha_P = 1.141 \pm 0.020(\text{stat}) \pm 0.044(\text{sys})$. Fitting both terms to the real photoproduction data (with $W^2 > 3 \text{ GeV}^2$) and BPC $\sigma_0^{\gamma p}$ data yields $\alpha_P = 1.101 \pm 0.002(\text{stat}) \pm 0.012(\text{sys})$. Including, in addition, the two direct measurements from HERA [34] gives $\alpha_P = 1.100 \pm 0.002(\text{stat}) \pm 0.012(\text{sys})$. At HERA energies the contribution of the Reggeon term is negligible. The values of α_P are compatible with the DL value of 1.08 and the recent best estimate of $1.0964^{+0.0115}_{-0.0094}$ by Cudell et al. [38].

⁵From studies of diffractive vector meson production and data on $R(= \sigma_L/\sigma_T)$ in inelastic ep scattering ξ is in the range 0.2 – 0.4 [16]. More recently ZEUS [35] has measured $ep \rightarrow epp$ at low Q^2 and found that R is about 0.4 at $Q^2 = 0.5 \text{ GeV}^2$.

The final step in the analysis of the BPC data is to combine the Q^2 dependence from the GVMD fit with the energy dependence from the Regge model

$$\sigma_{\text{tot}}^{\gamma^*p}(W^2, Q^2) = \left(\frac{M_0^2}{M_0^2 + Q^2} \right) (A_R(W^2)^{\alpha_R-1} + A_P(W^2)^{\alpha_P-1}). \quad (6)$$

The parameter M_0^2 is fixed to its value of 0.53 found above and α_R is also kept fixed at 0.5 as before. The 3 remaining parameters are determined by fitting to photoproduction data (with $W^2 > 3 \text{ GeV}^2$, but without the two original HERA measurements) and the measured BPC data. We find $A_R = 145.0 \pm 2.0 \mu\text{b}$, $A_P = 63.5 \pm 0.9 \mu\text{b}$ and $\alpha_P = 1.097 \pm 0.002$ with $\chi^2/ndf = 1.12$ (statistical errors only). If the two HERA photoproduction measurements are included the parameters do not change within their errors. The description of the low Q^2 F_2 data given by this model (ZEUSREGGE) is shown in Fig. 6. Data in the BPC region $Q^2 \leq 0.65 \text{ GeV}^2$ are well described. At larger Q^2 values the curves fall below the data. Including ZEUS SVX95 data at successively larger Q^2 values, we find that by $Q^2 = 3.5 \text{ GeV}^2$ the χ^2/ndf has increased to 1.7. Also shown in Fig. 6, for $Q^2 \geq 0.9 \text{ GeV}^2$, are the results of a NLO QCD fit (ZEUSQCD) described in Sec. 6.

To summarise, we have shown that the Q^2 dependence of the ZEUS BPC95 data at very low Q^2 can be described by a simple GVMD form. The resulting values of $\sigma_0^{\gamma^*p}$, the cross-sections extrapolated to $Q^2 = 0$, are somewhat larger than the direct measurements at HERA. A two component Regge model gives a good description of the W^2 dependence of the data, with a Pomeron intercept compatible with that determined from hadron-hadron data.

5 F_2 slopes

To quantify the low x behaviour of F_2 as a function of x and Q^2 , we calculate the slopes $d \ln F_2 / d \ln(1/x)$ at fixed Q^2 and $dF_2 / d \ln Q^2$ at fixed x from the ZEUS SVX95, BPC95 and ZEUS94 data sets. We use the ALLM97 parameterisation [39] for bin-centering F_2 data when necessary.

5.1 The slope $d \ln F_2 / d \ln(1/x)$

It is seen from Fig. 6 that the x slope of F_2 is small for small Q^2 and then starts to increase as Q^2 increases. At a fixed value of Q^2 and at small x the behaviour of F_2 can be characterised by $F_2 \propto x^{-\lambda_{eff}}$ (giving $\lambda_{eff} = d \ln F_2 / d \ln(1/x)$), with λ_{eff} taking rather different values in the Regge and LO BFKL approaches. The value of λ_{eff} as an observable at small x has been discussed by Navelet et al. [40, 41] and data on λ_{eff} with $x < 0.1$ have been presented by H1 [42].

Using statistical errors only, we fit F_2 data at fixed Q^2 and $x < 0.01$ to the form $Ax^{-\lambda_{eff}}$. Referring to Fig. 1, we are measuring λ_{eff} from horizontal slices of F_2 data between the $y = 1$ HERA kinematic limit and the fixed cut of $x < 0.01$. As the x range of the ZEUS BPC95 data is restricted we include data from E665 [32]. In each Q^2 bin the average value of x , $\langle x \rangle$, is calculated from the mean value of $\ln(1/x)$ weighted by the statistical errors of the corresponding F_2 values in that bin. For the estimation of the systematic errors, it is assumed that the systematic error analyses for each of the four data sets used

are independent. For a particular data set and a given systematic check, the F_2 points in each Q^2 bin are moved up and down by the respective systematic error estimates and the fits repeated, keeping all other data sets fixed at their nominal values. The positive and negative shifts with respect to the central values of λ_{eff} are added separately in quadrature to give the positive and negative systematic errors.

Fig. 7 shows the measured values of λ_{eff} as a function of Q^2 , and the data are given in Table 3 of the Appendix. At very low Q^2 the errors on λ_{eff} are large because this region is below the lower limit of E665 data (see Fig. 1). At $Q^2 > 100 \text{ GeV}^2$ the statistical error dominates. From the Regge approach of the previous section one would expect $\lambda_{eff} \approx 0.1$, independently of Q^2 . Data for $Q^2 < 1 \text{ GeV}^2$ are consistent with this expectation. The points labelled DL, linked by a dashed line, are calculated from the Donnachie-Landshoff prediction [22] and as expected from the discussion of the previous section are somewhat below the data. The variation of the DL points with Q^2 is a consequence of averaging the model in a Q^2 bin over a variable range of x and hence W^2 . For $Q^2 > 1 \text{ GeV}^2$, λ_{eff} increases to around 0.3 at Q^2 values of 40 GeV^2 . Qualitatively the tendency of λ_{eff} to increase with Q^2 is described by a number of pQCD approaches [41]. The points labelled GRV94, linked by a dashed line, are calculated from the NLO QCD GRV94 fit. Although the GRV94 prediction follows the trend of the data it tends to lie above the data, particularly in the Q^2 range $3 - 20 \text{ GeV}^2$. We shall return to this point later. For the predictions shown in Fig. 7 the same F_2 error weighted average in x at a given Q^2 is used as for the data.

5.2 The slope $dF_2/d \ln Q^2$

In QCD the scaling violations of F_2 are caused by gluon bremsstrahlung from quarks and quark pair creation from gluons. In the low x domain accessible at HERA the latter process dominates the scaling violations. F_2 is then largely determined by the sea quarks $F_2 \sim xS$, whereas the $dF_2/d \ln Q^2$ is dominated by the convolution of the splitting function P_{qg} and the gluon density: $dF_2/d \ln Q^2 \sim \alpha_S P_{qg} \otimes xg$. This has been used by Prytz [43] to relate xg directly to the measured values of $dF_2/d \ln Q^2$ [5]. The importance of $dF_2/d \ln Q^2$ as a tool for studying the low x region was pointed out by Bartels et al. [44].

In order to study the scaling violations of F_2 in more detail the logarithmic slope $dF_2/d \ln Q^2$ is derived from the data by fitting $F_2 = a + b \ln Q^2$ in bins of fixed x , using only statistical errors. The ZEUS data sets used are the BPC95, SVX95 and ZEUS94. For compatibility with our NLO QCD fit a cut of $W^2 > 10 \text{ GeV}^2$ is applied to the data. The F_2 data are shown in bins of x as functions of Q^2 in Fig. 8. The fits $F_2 = a + b \ln Q^2$ are also shown and the change of slope as x changes is visible from the plots. In each x bin the average value of Q^2 , $\langle Q^2 \rangle$, is derived from the F_2 statistical error weighted mean value of $\ln Q^2$ in that bin. Systematic errors on $dF_2/d \ln Q^2$ are estimated following the procedure outlined in the previous section. The results for $dF_2/d \ln Q^2$ as a function of x are shown in Fig. 9 and are given in Table 4 of the Appendix. The differences in the sizes of the errors on $dF_2/d \ln Q^2$ partially reflect the variations in Q^2 range as x varies (see Fig. 1 - we are taking vertical slices of the data to determine $dF_2/d \ln Q^2$). For values of x down to 3×10^{-4} , the slopes are increasing as x decreases. At lower values of x and Q^2 , the slopes decrease. If $dF_2/d \ln Q^2$ values are plotted for fixed target data at similar values of Q^2 , the ‘turn over’ is not seen, but the data are at larger values of

x [45, 46]. The points linked by the dashed lines are again from the DL Regge model and the GRV94 QCD fit, in both cases calculated using the same F_2 error weighted Q^2 averaging as for the data. The failure of DL is in line with our earlier discussion but the fact that GRV94 does not follow the trend of the data when it turns over is perhaps more surprising. Naively it appears that the GRV94 gluon density is too large even at Q^2 values around 5 GeV². We shall return to this discussion after we have presented the ZEUS NLO QCD fit to which we now turn.

6 NLO QCD fit to F_2 data and extraction of the gluon momentum density

In this section we present a NLO QCD fit to the ZEUS94 data [4] and the SVX95 data of this paper. We do not attempt a global fit to parton densities, but concentrate on what ZEUS data allow us to conclude about the behaviour of the gluon and quark densities at low x .

To constrain the fits at high x , proton and deuteron F_2 structure function data from NMC [47] and BCDMS [48] are included.⁶ The following cuts are made on the ZEUS and the fixed target data: (i) $W^2 > 10$ GeV² to reduce the sensitivity to target mass [49] and higher twist [50] contributions which become important at high x and low Q^2 ; (ii) discard deuteron data with $x > 0.7$ to eliminate possible contributions from Fermi motion in deuterium [51]. The kinematic range covered by the data input to the QCD fit is $3 \times 10^{-5} < x < 0.7$ and $1 < Q^2 < 5000$ GeV².

The QCD predictions for the F_2 structure functions are obtained by solving the DGLAP evolution equations [6] at NLO in the $\overline{\text{MS}}$ scheme [52]. These equations yield the quark and gluon momentum distributions (and thus the structure functions) at all values of Q^2 provided they are given as functions of x at some input scale Q_0^2 . In this analysis we adopt the so-called fixed flavour number scheme where only three light flavours (u, d, s) contribute to the quark density in the proton. In this scheme the assumption is made that the charm and bottom quarks are produced in the hard scattering process and the corresponding structure functions F_2^c and F_2^b are calculated from the photon-gluon fusion process including NLO corrections [53].

As will be explained later, the input scale is chosen to be $Q_0^2 = 7$ GeV². The gluon distribution (xg), the sea quark distribution (xS) and the difference of up and down quarks in the proton ($x\Delta_{ud}$) are parameterised as

$$\begin{aligned} xg(x, Q_0^2) &= A_g x^{\delta_g} (1-x)^{\eta_g} (1 + \gamma_g x) \\ xS(x, Q_0^2) &\equiv 2x(\bar{u} + \bar{d} + \bar{s}) = A_s x^{\delta_s} (1-x)^{\eta_s} (1 + \varepsilon_s \sqrt{x} + \gamma_s x) \\ x\Delta_{ud}(x, Q_0^2) &\equiv x(u + \bar{u}) - x(d + \bar{d}) = A_{\Delta} x^{\delta_{\Delta}} (1-x)^{\eta_{\Delta}}. \end{aligned} \quad (7)$$

The input valence distributions $xu_v = x(u - \bar{u})$ and $xd_v = x(d - \bar{d})$ at Q_0^2 are taken from the parton distribution set MRS(R2) [54]. As for MRS(R2) we assume that the strange quark distribution is a given fraction $K_s = 0.2$ of the sea at the scale

⁶Data from E665 are not included in the fit. They are important at low x and $Q^2 < 1$ GeV² but of much lower statistical weight at larger x compared to BCDMS and NMC. We have checked that including E665 data within the cuts described does not change the nominal fit result.

$Q^2 = 1 \text{ GeV}^2$. The gluon normalisation, A_g , is fixed by the momentum sum rule, $\int_0^1 (xg + xS + xu_v + xd_v)dx = 1$. There are thus 11 free parameters in the fit.

The input value for the strong coupling constant is set to $\alpha_s(M_Z^2) = 0.118$ [55]. With a charm (bottom) threshold of $Q_{c(b)} = 1.5$ (5) GeV this corresponds to values of the QCD scale parameter $\Lambda_{\overline{\text{MS}}} = (404, 343, 243)$ MeV for $f = (3, 4, 5)$ flavours. In the calculation of the charm structure function F_2^c the charm mass is taken to be $m_c = 1.5$ GeV; the contribution from bottom is found to be negligible in the kinematic range covered by the data. In the QCD evolutions and the evaluation of the structure functions the renormalisation scale and the mass factorisation scale are both set equal to Q^2 .

The QCD evolutions and the structure function calculations are done with the program QCDNUM [56]. The QCD evolution equations are written in terms of quark flavour singlet and non-singlet and gluon momentum distributions. The quark non-singlet evolution is independent of the gluon. The quark singlet distribution is defined as the sum over all quark and anti-quark distributions

$$x\Sigma = \sum_{i=u,d,s} [xq_i(x) + x\bar{q}_i(x)] \quad (8)$$

and its evolution in Q^2 is coupled to that of the gluon distribution. At small values of x , $x\Sigma$ is dominated by the contribution from the $q\bar{q}$ sea xS . Note that for data with $Q^2 < Q_0^2 = 7 \text{ GeV}^2$, backwards evolutions in Q^2 are performed. The χ^2 minimisation and the calculation of the covariance matrices are based on MINUIT [57]. In the definition of the χ^2 only statistical errors are included and the relative normalisations of the data sets are fixed at unity.

The fit yields a good description of the data as shown in Fig. 10 where we plot the Q^2 dependence of the proton structure function F_2 in the x range covered by the ZEUS94 data. The characteristic pattern of scaling violations can be seen clearly from this plot, with F_2 at low values of x rising as Q^2 increases. The quality of the fit to ZEUS data at low Q^2 is also shown by the full line in Fig. 3. Adding the statistical and systematic errors in quadrature gives a χ^2 of 1474 for 1120 data points and 11 free parameters. We have also checked that the gluon obtained from this fit to scaling violations gives values of F_2^c in agreement with the ZEUS measurements [58]. The values of the fitted parameters are given in Table 5 of the Appendix.

Fig. 11 shows the gluon momentum distribution as a function of x for Q^2 at 1, 7 and 20 GeV^2 . The following sources contribute to the inner shaded error bands displayed in the figure (for each source we give in brackets the relative error $\Delta g/g$ at $x = 5 \times 10^{-5}$, $Q^2 = 7 \text{ GeV}^2$):

1. The statistical error on the data (4%).
2. The experimental systematic errors, (13%), which are propagated to the covariance matrix of the fitted parameters using the technique described in [59]. In total 26 independent sources of systematic error are included. Proper account is taken of the correlations between the systematic errors of the NMC datasets and for BCDMS the procedure of [50] is followed. Normalisation errors of all data sets are also included.

3. The uncertainties on the strong coupling constant $\Delta\alpha_s(M_Z^2) = 0.005$ (8%), on the strange quark content of the proton $\Delta K_s = 0.1$ (1%) and on the charm mass $\Delta m_c = 0.2$ GeV (1%).

Adding errors from (1), (2) and (3) together in quadrature gives a total contribution of 16%.⁷

In addition to the above sources of error a ‘parameterisation error’ (10%) is obtained by repeating the fit with:

4. The addition of statistical and systematic errors in quadrature in the definition of the χ^2 instead of taking statistical errors only.
5. The input scale set to $Q_0^2 = 1$ and 4 GeV² instead of 7 GeV².
6. An alternative parameterisation of the gluon density:

$$xg(x, Q_0^2) = A_g(1-x)^{\eta_g} \left[1 + \sum_{n=1}^3 C_n T_n(y) \right] \quad (9)$$

where $T_n(y)$ is a Chebycheff polynomial of the first kind [60] and $y = a \ln x + b$ with the coefficients a, b adjusted such that $x \in [10^{-6}, 1]$ maps onto $y \in [-1, 1]$. This parameterisation is flexible enough to describe the rapid change with Q^2 (see Fig. 11) of the shape of the gluon density. Furthermore, Eq. (9) allows the gluon density to become negative at low x whereas Eq. (7) imposes the constraint $xg(x) \geq 0$ as $x \rightarrow 0$.

Taking all combinations of the alternatives described in 4., 5. and 6. above in addition to the nominal settings, twelve fits are performed and the parameterisation error is defined as the envelope of the resulting set of quark and gluon distributions. All these fits yield similar values of χ^2 . The nominal fit (ZEUSQCD) is taken to be that which gives a curve that is roughly at the centre of the error bands for all x and Q^2 . This also defines the choice of $Q_0^2 = 7$ GeV². The outer hatched error bands in Fig. 11 correspond to the total error now including the parameterisation error added in quadrature with the other errors. At $x = 5 \times 10^{-5}$, $Q^2 = 7$ GeV² the total $\Delta g/g = 19\%$.

The three left-hand plots of Fig. 12 show the distributions for $x\Sigma$ and xg as functions of x for Q^2 at 1, 7 and 20 GeV². The error bands shown correspond to the quadratic sum of all error sources. It can be seen that even at the smallest Q^2 the quark singlet distribution, $x\Sigma$, is rising at small x whereas the gluon distribution, xg , has become almost flat, indeed compatible with zero. This behaviour has also been found by others, for instance Martin et al. (MRST) [46] in their recent global determination of parton densities. At $Q^2 = 1$ GeV² the gluon distribution is poorly determined and can, within errors, be negative at low x . In the simplest form of the parton model (and leading order QCD) this would clearly be unphysical and while it is known that at NLO in the $\overline{\text{MS}}$ scheme a positive parton density will remain positive for forward evolution in Q^2 there is no such constraint for backwards evolution [61]. A negative gluon distribution is therefore not necessarily in contradiction with perturbative NLO QCD provided cross-sections or structure functions calculated from the parton distributions are positive for

⁷This combination of errors (‘HERA standard errors’) is often used by the H1 and ZEUS experiments when discussing xg .

all x and Q^2 in the fitted kinematic domain. We have verified that this is the case for F_2^c and the longitudinal structure function F_L .⁸

7 The transition region and NLO QCD

7.1 The NLO QCD fit at low Q^2

It is now widely observed that NLO DGLAP QCD fits give good descriptions of F_2 data down to Q^2 values in the range $1 - 2 \text{ GeV}^2$. For such fits to be valid one assumes:

1. the validity of the DGLAP QCD formalism;
2. NLO is sufficient even though α_S is becoming large (e.g. for this analysis $\alpha_S = 0.46$ at 1 GeV^2);
3. that no higher twist terms, shadowing or other non-perturbative effects contribute to F_2 .

In this paper we have also deliberately made the minimum of assumptions about the low x functional form of the parton distributions at Q_0^2 . We require only that they must tend to zero as $x \rightarrow 1$ and that the flavour and momentum sum-rules are respected.

To investigate the stability of our results at low Q^2 we have repeated the full QCD fit and error evaluation procedure on the same data as in Sec. 6 but with the minimum Q^2 cut (Q_{min}^2) raised to 4 GeV^2 . The quality of the fit is much as before, χ^2 of 1242 for 943 data points and 11 parameters (statistical and systematic errors added in quadrature). The resulting $x\Sigma$ and xg parton distributions are shown in the three right-hand plots of Fig. 12. Qualitatively the features shown by the standard fit (left-hand plots) are unchanged. The rising $x\Sigma$ distribution at low x remains and the sea dominates the gluon at small x and the lowest Q^2 value. In more detail:

- The parton densities from the central fits with $Q_{min}^2 = 1$ and 4 GeV^2 are very similar.
- Except at the lowest Q^2 , the precision of the determination of $x\Sigma$ is not much reduced. Even at $Q^2 = 1 \text{ GeV}^2$, $x\Sigma$ is reasonably well determined for $x > 3 \times 10^{-4}$, at smaller x values there are insufficient data to constrain the fit.
- At all Q^2 values shown in the right-hand plots the precision of the determination of xg for $x < 10^{-3}$ is worse.

The increase in the error bands for the gluon density when the Q_{min}^2 cut is increased shows the importance of the SVX95 data at low x and low Q^2 in determining xg in this region.

To investigate if there is a technical lower limit to the NLO QCD fit (in the sense that the fit fails to converge or gives a very bad χ^2), we extend the QCD fit into the region covered by the ZEUS BPC95 data by lowering the Q_{min}^2 cut to 0.4 GeV^2 . The fit gives an acceptable description of the data with F_2^c positive and F_L (calculated as in [62]) only slightly negative at $x \approx 5 \times 10^{-3}$ and $Q^2 = 0.5 \text{ GeV}^2$. We therefore conclude that we do

⁸Here and in the following F_L is calculated using the QCD calculation of Altarelli and Martinelli [62].

not observe a significant breakdown of the NLO DGLAP description in the kinematic range explored. However, we stress that, within the present experimental accuracy, F_2 data by itself cannot validate the assumptions noted at the beginning of this section and that other information such as precise measurements of F_2^c in DIS, measurements of other hard processes or more theoretical input is required.⁹

7.2 F_2 slopes and models

In order to clarify what we have learned about the transition region from the ZEUS Regge fit and the NLO DGLAP fits we return to the F_2 slopes.

Fig. 7, showing the ZEUS+E665 λ_{eff} data of Sec. 5.1, also shows the calculation from the ZEUSREGGE fit of Sec. 4 and for $Q^2 > 1 \text{ GeV}^2$ the result from the ZEUSQCD fit of Sec. 6. In the BPC region, the ZEUSREGGE (full line) calculation gives λ_{eff} somewhat higher than that given by the original DL Regge fit (dashed line), but it is still below the data. This is largely because the ZEUSREGGE fit includes low W photoproduction data and thus gives a lower α_P than the value of 1.141 from the Regge fit to the extrapolated ZEUS BPC σ_0^{7p} data alone. At larger Q^2 values, ZEUSQCD (full line) gives a good account of the trend and normalisation of λ_{eff} while GRV94 (dashed line) tends to predict a larger value of λ_{eff} , which means a steeper rise of F_2 as x decreases, than that determined from the data.

Fig. 9 shows the ZEUS $dF_2/d\ln Q^2$ data together with the same two calculations, ZEUSREGGE at very low x and Q^2 values and ZEUSQCD for $Q^2 > 1 \text{ GeV}^2$. The ZEUSREGGE points show much the same trend as that of the original DL model. At Q^2 values between 1 and 5 GeV^2 , the ZEUSQCD points are qualitatively different from those of GRV94. The ZEUSQCD values now follow the ‘turn over’ of the slope data around $x \sim 3 \times 10^{-4}$. This has also been found by MRST in [46] where they compare their global fit to $dF_2/d\ln Q^2$ data from H1, ZEUS and the NMC experiments. The rise in F_2 at low x and the ‘turn over’ in $dF_2/d\ln Q^2$ reflect the different behaviours of the gluon and $q\bar{q}$ sea distributions at $Q^2 \sim 1 \text{ GeV}^2$. For very small x the sea continues to rise ($\delta_s < 0$ in the notation of Eq. (7)) whereas the gluon rises significantly less steeply or even tends to zero ($\delta_g \geq 0$).

In contrast, for the GRV94 parton densities GRV assume that at their low starting scale of 0.34 GeV^2 *both* the gluon and the sea distributions are non-singular. All the rise of F_2 at low x for $Q^2 > 1 \text{ GeV}^2$ is then generated through the DGLAP evolution equations. In a recent paper GRV [64] have revisited their ‘dynamical parton model’ in the light of the HERA 1994 data and have produced a new set of parton distributions – GRV98. They find that they can correct most of the discrepancies between GRV94 and the HERA data by a slight increase in the starting scale from 0.34 to 0.4 GeV^2 and by using a lower value of $\alpha_S(M_Z^2) = 0.114$ rather than the value of 0.118 used in the ZEUS NLO QCD fit. They acknowledge that if they use a larger value of α_S then their starting scale has to be increased to around 1 GeV^2 and they have to accept a rising $q\bar{q}$ sea distribution at the starting scale.

⁹Some of the features that we find, such as the suppression of the gluon density at small Q^2 , and the ability of the NLO DGLAP formalism to fit very low Q^2 data have been noted previously by Lopez et al. [63].

8 Summary and conclusions

In this paper we have presented the measurement by ZEUS of F_2 in the Q^2 region $0.6 - 17 \text{ GeV}^2$ (SVX95), which fills the gap between the very low Q^2 BPC95 data ($0.11 - 0.65 \text{ GeV}^2$) and the large 1994 data sample ($3.5 - 5000 \text{ GeV}^2$). We have shown that the BPC data may be described successfully by non-perturbative approaches: a simple generalised vector dominance model for the Q^2 dependence and a two component Regge model for the W^2 dependence. For $Q^2 \geq 0.9 \text{ GeV}^2$ these approaches fail to describe the dominant feature of the data, which is the rapid rise of F_2 at small x .

We have studied the transition region by fitting $F_2 = Ax^{-\lambda_{eff}}$ using ZEUS and E665 data with $x < 0.01$ in the Q^2 range $0.15 - 250 \text{ GeV}^2$. For $Q^2 > 0.9 \text{ GeV}^2$ the data are not compatible with the Q^2 independence of λ_{eff} , as expected for a dominant Pomeron term in conventional Regge theory, but are well described by the ZEUS NLO QCD fit. The slope $dF_2/d\ln Q^2$ has been calculated from ZEUS F_2 data in the range $2 \times 10^{-6} < x < 0.2$. Assuming pQCD, F_2 at low x is largely determined by the $q\bar{q}$ sea density whereas $dF_2/d\ln Q^2$ is given by the gluon density. As x decreases the slope values increase until at $x \approx 3 \times 10^{-4}$ there is a turn over and for smaller x values the slope values decrease.

To study the behaviour of the parton densities in more detail we have performed a NLO DGLAP QCD fit to ZEUS and fixed target data with $Q^2 > 1 \text{ GeV}^2$ and $3 \times 10^{-5} < x < 0.7$. A good description of the F_2 data over the whole range of Q^2 from 1 to 5000 GeV^2 is obtained. Around the lower Q^2 limit of the fit we find that the $q\bar{q}$ sea distribution is still rising at small x , whereas the gluon distribution is strongly suppressed. These findings are incompatible with the hypothesis that the rapid rise in F_2 is driven by the rapid increase in gluon density at small x from parton splitting alone. These features remain true if the lowest Q^2 for which data is included in the fit is raised from 1 to 4 GeV^2 .

From the ZEUS QCD fit we also obtain a much improved determination of the gluon momentum density compared to the previous determination by ZEUS [5]. Full account has been taken of correlated experimental systematic errors and the uncertainty in the form of the input gluon distribution function has also been estimated. At $Q^2 = 20 \text{ GeV}^2$ and $x = 5 \times 10^{-5}$ the total fractional error on the gluon density has been reduced from 40% to 10%.

We have used NLO pQCD and the simplest non-perturbative models to study the transition region in Q^2 . We find, for $Q^2 \geq 0.9 \text{ GeV}^2$, that the wholly non-perturbative description fails. Although pQCD may not be valid at such low scales, we have not been able to find a lower limit at which the NLO DGLAP fit breaks down conclusively.

Acknowledgements

The experiment was made possible by the skill and dedication of the HERA machine group who ran HERA most efficiently during 1994 and 1995 when the data for this paper were collected. The realisation and continuing operation of the ZEUS detector has been and is made possible by the inventiveness and continuing hard work of many people not listed as authors. Their contributions are acknowledged with great appreciation. The support and encouragement of the DESY directorate continues to be invaluable for the

successful operation of the ZEUS collaboration. We thank J. Blümlein, R. Thorne and W. J. Stirling for discussions on QCD.

Appendix

The following tables are also available via the ZEUS collaboration home page, <http://www-zeus.desy.de/>. Fortran routines and data files to calculate the parton distributions from the ZEUS NLO QCD fits are also available from this site.

bin	x	Q^2 (GeV ²)	F_2	error $stat.$ ^{+sys} _{-sys}	F_2 ($F_L = 0$)
1	$1.2 \cdot 10^{-5}$	0.6	0.531	$\pm 0.030^{+0.037}_{-0.060}$	0.517
2	$1.9 \cdot 10^{-5}$	0.9	0.653	$\pm 0.030^{+0.067}_{-0.053}$	0.632
3	$2.6 \cdot 10^{-5}$	0.9	0.655	$\pm 0.023^{+0.039}_{-0.037}$	0.644
4	$3.6 \cdot 10^{-5}$	0.9	0.574	$\pm 0.022^{+0.034}_{-0.050}$	0.570
5	$2.8 \cdot 10^{-5}$	1.3	0.716	$\pm 0.029^{+0.069}_{-0.065}$	0.687
6	$3.8 \cdot 10^{-5}$	1.3	0.717	$\pm 0.023^{+0.043}_{-0.037}$	0.703
7	$5.3 \cdot 10^{-5}$	1.3	0.715	$\pm 0.022^{+0.036}_{-0.041}$	0.708
8	$8.0 \cdot 10^{-5}$	1.3	0.626	$\pm 0.017^{+0.033}_{-0.031}$	0.624
9	$1.6 \cdot 10^{-4}$	1.3	0.559	$\pm 0.016^{+0.046}_{-0.047}$	0.558
10	$3.9 \cdot 10^{-5}$	1.9	0.915	$\pm 0.036^{+0.071}_{-0.070}$	0.873
11	$5.3 \cdot 10^{-5}$	1.9	0.852	$\pm 0.028^{+0.033}_{-0.051}$	0.833
12	$7.5 \cdot 10^{-5}$	1.9	0.742	$\pm 0.025^{+0.038}_{-0.026}$	0.734
13	$1.1 \cdot 10^{-4}$	1.9	0.740	$\pm 0.023^{+0.035}_{-0.038}$	0.736
14	$2.2 \cdot 10^{-4}$	1.9	0.636	$\pm 0.019^{+0.026}_{-0.057}$	0.635
15	$5.4 \cdot 10^{-5}$	2.5	0.964	$\pm 0.039^{+0.060}_{-0.060}$	0.916
16	$7.3 \cdot 10^{-5}$	2.5	0.909	$\pm 0.029^{+0.044}_{-0.040}$	0.887
17	$1.0 \cdot 10^{-4}$	2.5	0.870	$\pm 0.027^{+0.022}_{-0.044}$	0.860
18	$1.6 \cdot 10^{-4}$	2.5	0.771	$\pm 0.023^{+0.050}_{-0.016}$	0.767
19	$3.0 \cdot 10^{-4}$	2.5	0.725	$\pm 0.023^{+0.029}_{-0.060}$	0.724
20	$7.3 \cdot 10^{-5}$	3.5	1.140	$\pm 0.050^{+0.058}_{-0.057}$	1.081
21	$9.8 \cdot 10^{-5}$	3.5	0.995	$\pm 0.035^{+0.040}_{-0.023}$	0.970
22	$1.4 \cdot 10^{-4}$	3.5	0.945	$\pm 0.031^{+0.034}_{-0.022}$	0.933
23	$2.1 \cdot 10^{-4}$	3.5	0.839	$\pm 0.026^{+0.019}_{-0.028}$	0.834
24	$4.1 \cdot 10^{-4}$	3.5	0.663	$\pm 0.021^{+0.044}_{-0.048}$	0.661
25	$1.0 \cdot 10^{-4}$	4.5	1.160	$\pm 0.043^{+0.040}_{-0.044}$	1.108
26	$1.7 \cdot 10^{-4}$	4.5	1.005	$\pm 0.031^{+0.050}_{-0.037}$	0.990
27	$2.8 \cdot 10^{-4}$	4.5	0.912	$\pm 0.030^{+0.029}_{-0.032}$	0.907
28	$5.4 \cdot 10^{-4}$	4.5	0.664	$\pm 0.022^{+0.055}_{-0.057}$	0.663
29	$1.4 \cdot 10^{-4}$	6	1.305	$\pm 0.055^{+0.041}_{-0.037}$	1.247
30	$2.2 \cdot 10^{-4}$	6	1.086	$\pm 0.039^{+0.025}_{-0.046}$	1.070
31	$3.7 \cdot 10^{-4}$	6	1.002	$\pm 0.038^{+0.027}_{-0.033}$	0.996
32	$7.1 \cdot 10^{-4}$	6	0.753	$\pm 0.028^{+0.050}_{-0.079}$	0.751
33	$1.8 \cdot 10^{-4}$	7.5	1.210	$\pm 0.058^{+0.037}_{-0.051}$	1.167
34	$3.6 \cdot 10^{-4}$	7.5	0.918	$\pm 0.036^{+0.074}_{-0.023}$	0.910
35	$8.8 \cdot 10^{-4}$	7.5	0.810	$\pm 0.040^{+0.060}_{-0.038}$	0.808
36	$2.2 \cdot 10^{-4}$	9	1.296	$\pm 0.061^{+0.039}_{-0.074}$	1.251
37	$4.3 \cdot 10^{-4}$	9	0.957	$\pm 0.038^{+0.028}_{-0.036}$	0.948
38	$1.1 \cdot 10^{-3}$	9	0.818	$\pm 0.039^{+0.027}_{-0.065}$	0.816
39	$2.8 \cdot 10^{-4}$	12	1.306	$\pm 0.057^{+0.066}_{-0.038}$	1.265
40	$5.6 \cdot 10^{-4}$	12	1.084	$\pm 0.040^{+0.043}_{-0.061}$	1.073
41	$1.4 \cdot 10^{-3}$	12	0.956	$\pm 0.044^{+0.057}_{-0.040}$	0.954
42	$3.9 \cdot 10^{-4}$	17	1.311	$\pm 0.057^{+0.040}_{-0.055}$	1.270
43	$7.9 \cdot 10^{-4}$	17	1.087	$\pm 0.038^{+0.051}_{-0.041}$	1.077
44	$1.9 \cdot 10^{-3}$	17	0.931	$\pm 0.045^{+0.046}_{-0.077}$	0.927

Table 1: Values of x , Q^2 , F_2 , statistical and systematic errors from the ZEUS 1995 shifted vertex analysis (SVX95).

bin	W [GeV]	ϵ	$\sigma_0^{\gamma p}$ [μb]	stat. err. [μb]	sys. err. [μb]
1	104	0.99	156.2	± 5.3	± 16.1
2	134	0.98	166.1	± 5.2	± 11.0
3	153	0.96	174.7	± 4.9	± 12.9
4	173	0.92	175.5	± 5.0	± 11.7
5	190	0.88	181.8	± 4.7	± 12.8
6	212	0.80	186.8	± 4.8	± 13.5
7	233	0.69	192.5	± 4.7	± 13.3
8	251	0.55	204.8	± 5.6	± 17.0

Table 2: Values of $\sigma_0^{\gamma p}$ together with statistical and systematic errors from the GVMD extrapolation, with $\sigma_L = 0$, of ZEUS BPC95 data. W is the γ^*p centre-of-mass energy and ϵ is the polarisation of the virtual photon.

bin	Q^2 (GeV ²)	x_{min}	x_{max}	$\langle x \rangle$	λ_{eff}	error stat. $^{+sys}_{-sys}$
1	0.15	$2.4 \cdot 10^{-6}$	$4.2 \cdot 10^{-6}$	$3.2 \cdot 10^{-6}$	0.134	$\pm 0.077^{+0.189}_{-0.194}$
2	0.2	$3.2 \cdot 10^{-6}$	$8.5 \cdot 10^{-6}$	$5.5 \cdot 10^{-6}$	0.128	$\pm 0.036^{+0.080}_{-0.083}$
3	0.25	$4.6 \cdot 10^{-6}$	$1.8 \cdot 10^{-3}$	$1.3 \cdot 10^{-5}$	0.136	$\pm 0.016^{+0.040}_{-0.044}$
4	0.3	$6.7 \cdot 10^{-6}$	$2.5 \cdot 10^{-3}$	$1.1 \cdot 10^{-4}$	0.110	$\pm 0.007^{+0.017}_{-0.022}$
5	0.4	$1.1 \cdot 10^{-5}$	$5.2 \cdot 10^{-3}$	$6.8 \cdot 10^{-4}$	0.115	$\pm 0.005^{+0.015}_{-0.019}$
6	0.5	$2.1 \cdot 10^{-5}$	$4.6 \cdot 10^{-5}$	$2.9 \cdot 10^{-5}$	0.193	$\pm 0.050^{+0.100}_{-0.097}$
7	0.65	$1.2 \cdot 10^{-5}$	$5.2 \cdot 10^{-3}$	$1.8 \cdot 10^{-3}$	0.114	$\pm 0.007^{+0.016}_{-0.019}$
8	0.9	$1.9 \cdot 10^{-5}$	$8.9 \cdot 10^{-3}$	$3.8 \cdot 10^{-3}$	0.147	$\pm 0.005^{+0.013}_{-0.014}$
9	1.3	$2.8 \cdot 10^{-5}$	$8.9 \cdot 10^{-3}$	$2.4 \cdot 10^{-3}$	0.152	$\pm 0.006^{+0.014}_{-0.014}$
10	1.9	$3.9 \cdot 10^{-5}$	$8.9 \cdot 10^{-3}$	$1.8 \cdot 10^{-3}$	0.160	$\pm 0.008^{+0.014}_{-0.013}$
11	2.5	$5.4 \cdot 10^{-5}$	$8.9 \cdot 10^{-3}$	$1.3 \cdot 10^{-3}$	0.179	$\pm 0.010^{+0.016}_{-0.014}$
12	3.5	$6.3 \cdot 10^{-5}$	$8.9 \cdot 10^{-3}$	$6.1 \cdot 10^{-4}$	0.178	$\pm 0.012^{+0.022}_{-0.018}$
13	4.5	$1.0 \cdot 10^{-4}$	$5.4 \cdot 10^{-4}$	$2.0 \cdot 10^{-4}$	0.261	$\pm 0.020^{+0.042}_{-0.041}$
14	6.5	$1.0 \cdot 10^{-4}$	$4.0 \cdot 10^{-3}$	$7.9 \cdot 10^{-4}$	0.192	$\pm 0.005^{+0.016}_{-0.012}$
15	8.5	$1.6 \cdot 10^{-4}$	$1.6 \cdot 10^{-3}$	$6.7 \cdot 10^{-4}$	0.261	$\pm 0.012^{+0.016}_{-0.020}$
16	10	$1.6 \cdot 10^{-4}$	$6.3 \cdot 10^{-3}$	$1.6 \cdot 10^{-3}$	0.226	$\pm 0.007^{+0.015}_{-0.014}$
17	12	$2.5 \cdot 10^{-4}$	$2.5 \cdot 10^{-3}$	$9.7 \cdot 10^{-4}$	0.250	$\pm 0.014^{+0.018}_{-0.020}$
18	15	$2.5 \cdot 10^{-4}$	$6.3 \cdot 10^{-3}$	$1.9 \cdot 10^{-3}$	0.249	$\pm 0.010^{+0.016}_{-0.014}$
19	18	$3.9 \cdot 10^{-4}$	$6.3 \cdot 10^{-3}$	$2.1 \cdot 10^{-3}$	0.274	$\pm 0.010^{+0.014}_{-0.013}$
20	22	$4.0 \cdot 10^{-4}$	$1.0 \cdot 10^{-2}$	$3.4 \cdot 10^{-3}$	0.273	$\pm 0.010^{+0.017}_{-0.014}$
21	27	$6.3 \cdot 10^{-4}$	$6.3 \cdot 10^{-3}$	$2.7 \cdot 10^{-3}$	0.332	$\pm 0.015^{+0.017}_{-0.014}$
22	35	$6.3 \cdot 10^{-4}$	$1.0 \cdot 10^{-2}$	$3.7 \cdot 10^{-3}$	0.308	$\pm 0.016^{+0.013}_{-0.019}$
23	45	$1.0 \cdot 10^{-3}$	$1.0 \cdot 10^{-2}$	$3.7 \cdot 10^{-3}$	0.289	$\pm 0.020^{+0.022}_{-0.017}$
24	60	$1.0 \cdot 10^{-3}$	$1.0 \cdot 10^{-2}$	$4.7 \cdot 10^{-3}$	0.342	$\pm 0.021^{+0.009}_{-0.017}$
25	70	$1.6 \cdot 10^{-3}$	$1.0 \cdot 10^{-2}$	$4.8 \cdot 10^{-3}$	0.306	$\pm 0.032^{+0.018}_{-0.023}$
26	90	$1.6 \cdot 10^{-3}$	$1.0 \cdot 10^{-2}$	$5.3 \cdot 10^{-3}$	0.273	$\pm 0.040^{+0.046}_{-0.027}$
27	120	$2.5 \cdot 10^{-3}$	$1.0 \cdot 10^{-2}$	$6.2 \cdot 10^{-3}$	0.380	$\pm 0.059^{+0.001}_{-0.002}$
28	150	$2.5 \cdot 10^{-3}$	$1.0 \cdot 10^{-2}$	$6.3 \cdot 10^{-3}$	0.258	$\pm 0.079^{+0.004}_{-0.004}$
29	200	$4.0 \cdot 10^{-3}$	$1.0 \cdot 10^{-2}$	$7.0 \cdot 10^{-3}$	0.250	$\pm 0.126^{+0.009}_{-0.003}$
30	250	$4.0 \cdot 10^{-3}$	$1.0 \cdot 10^{-2}$	$7.9 \cdot 10^{-3}$	0.452	$\pm 0.184^{+0.008}_{-0.000}$

Table 3: Values of the slope $\lambda_{eff} = d \ln F_2 / d \ln(1/x)$ and their errors, calculated from fitting $F_2 = Ax^{-\lambda_{eff}}$ at fixed Q^2 to ZEUS and E665 data with $x < 0.01$. The columns labelled x_{min}, x_{max} and $\langle x \rangle$ give the minimum, maximum and average values of x in a bin. $\langle x \rangle$ is calculated as described in Sec. 5.1 of the text.

bin	x	Q_{min}^2 (GeV ²)	Q_{max}^2	$\langle Q^2 \rangle$	$dF_2/d\ln Q^2$	error $stat.$ $^{+sys}_{-sys}$
1	$2.1 \cdot 10^{-6}$	0.11	0.15	0.12	0.135	$\pm 0.029^{+0.030}_{-0.029}$
2	$3.1 \cdot 10^{-6}$	0.15	0.2	0.16	0.198	$\pm 0.028^{+0.033}_{-0.033}$
3	$4.6 \cdot 10^{-6}$	0.15	0.25	0.2	0.174	$\pm 0.017^{+0.047}_{-0.047}$
4	$7.3 \cdot 10^{-6}$	0.2	0.3	0.23	0.191	$\pm 0.019^{+0.040}_{-0.040}$
5	$1.2 \cdot 10^{-5}$	0.25	0.6	0.29	0.265	$\pm 0.017^{+0.020}_{-0.023}$
6	$2.0 \cdot 10^{-5}$	0.3	0.9	0.37	0.297	$\pm 0.018^{+0.026}_{-0.022}$
7	$3.3 \cdot 10^{-5}$	0.3	1.9	0.52	0.312	$\pm 0.009^{+0.032}_{-0.031}$
8	$6.3 \cdot 10^{-5}$	0.5	3.5	1.1	0.365	$\pm 0.010^{+0.032}_{-0.032}$
9	$1.0 \cdot 10^{-4}$	1.3	6.5	2.5	0.379	$\pm 0.018^{+0.049}_{-0.043}$
10	$1.6 \cdot 10^{-4}$	1.3	10	3.8	0.387	$\pm 0.013^{+0.038}_{-0.038}$
11	$2.5 \cdot 10^{-4}$	1.9	15	5.2	0.368	$\pm 0.013^{+0.043}_{-0.029}$
12	$4.0 \cdot 10^{-4}$	3.5	22	8.8	0.429	$\pm 0.018^{+0.044}_{-0.035}$
13	$6.3 \cdot 10^{-4}$	4.5	35	10	0.404	$\pm 0.015^{+0.040}_{-0.035}$
14	$1.0 \cdot 10^{-3}$	6.5	60	13	0.315	$\pm 0.014^{+0.018}_{-0.020}$
15	$1.6 \cdot 10^{-3}$	6.5	90	14	0.262	$\pm 0.012^{+0.015}_{-0.012}$
16	$2.5 \cdot 10^{-3}$	6.5	150	19	0.227	$\pm 0.009^{+0.011}_{-0.017}$
17	$4.0 \cdot 10^{-3}$	6.5	250	26	0.139	$\pm 0.008^{+0.019}_{-0.007}$
18	$6.3 \cdot 10^{-3}$	10	450	24	0.150	$\pm 0.008^{+0.015}_{-0.008}$
19	$1.0 \cdot 10^{-2}$	22	800	56	0.119	$\pm 0.012^{+0.022}_{-0.018}$
20	$1.6 \cdot 10^{-2}$	6.5	1200	19	0.059	$\pm 0.005^{+0.011}_{-0.022}$
21	$2.5 \cdot 10^{-2}$	22	1500	45	0.061	$\pm 0.008^{+0.020}_{-0.010}$
22	$4.0 \cdot 10^{-2}$	6.5	2000	167	0.037	$\pm 0.007^{+0.019}_{-0.045}$
23	$8.1 \cdot 10^{-2}$	10	5000	156	0.018	$\pm 0.004^{+0.016}_{-0.022}$
24	0.2	90	5000	388	0.008	$\pm 0.010^{+0.005}_{-0.010}$

Table 4: Values of the slope $dF_2/d\ln Q^2$ and their errors calculated from fitting ZEUS F_2 data to the form $a + b\ln Q^2$. The columns labelled Q_{min}^2, Q_{max}^2 and $\langle Q^2 \rangle$ give the minimum, maximum and average values of Q^2 in a bin. $\langle Q^2 \rangle$ is calculated as described in Sec. 5.2 of the text.

Parameter	$xg(x)$	$xS(x)$	$x\Delta_{ud}(x)$
A	1.77	0.520	6.07
δ	-0.225	-0.241	1.27
η	9.07	8.60	3.68
ε		0.290	
γ	3.00	8.27	

Table 5: Values for the parameters of the nominal ZEUS NLO QCD fit (ZEUSQCD) at the starting scale $Q_0^2 = 7 \text{ GeV}^2$. The parameters are defined in Eq. (7) of the text.

References

- [1] ZEUS Collaboration, M. Derrick et al., Phys. Lett. B316 (1993) 412; Z. Phys. C65 (1995) 379; ibid C69 (1996) 607; ibid C72 (1996) 399.
H1 Collaboration, I. Abt et al., Nucl. Phys. B407 (1993) 515; T. Ahmed et al., Nucl. Phys. B439 (1995) 471; H. Aid et al., Nucl. Phys. B470 (1996) 3.
- [2] ZEUS Collaboration, J. Breitweg et al., Phys. Lett. B407 (1997) 432..
- [3] ZEUS Collaboration, M. Derrick et al., Z.Phys. C69 (1996) 607.
- [4] ZEUS Collaboration, M. Derrick et al., Z.Phys. C72 (1996) 399.
- [5] ZEUS Collaboration, M. Derrick et al., Phys. Lett. B345 (1995) 576.
- [6] G. Parisi, Proc 11th Rencontre de Morionde (1976);
G. Altarelli & G. Parisi, Nucl. Phys. B126 (1977) 298;
V. Gribov & L. Lipatov, Sov. Jour. Nucl. Phys. 15 (1972) 438;
L. Lipatov, Sov. Jour. Nucl. Phys. 20 (1975) 94;
Y. Dokshitzer, Sov. Phys. JETP 46 (1977) 641;
- [7] M. Glück, E. Reya & A. Vogt, Z.Phys. C48 (1990) 471; C53 (1992) 127.
- [8] M. Glück, E. Reya & A. Vogt, Z.Phys. C67 (1995) 433.
- [9] Y. Balitzki & L. Lipatov, Sov. Jour. Nucl. Phys. 28 (1978) 822;
E. Kuraev, L. Lipatov & V. Fadin, Sov. Phys. JETP 45 (1977) 199.
- [10] V.S. Fadin & L.N. Lipatov, hep-ph/9802290;
M. Ciafaloni & G. Camici, hep-ph/9803389.
- [11] D.A. Ross, SHEP-98/06 hep-ph/9804332;
Y.V. Kovchegov & A.H. Mueller, CU-TP-889 hep-ph/9805208;
E.M. Levin, TAUP 2501-98 hep-ph/9806228;
J. Blümlein et al., DESY 98-036, WUE-ITP-98-017, hep-ph/9806368.
- [12] Proc. of the Int'l Workshop on DIS, Rome 1996, eds A. Negri & G. D'Agostini;
Proc. of the Int'l Workshop on DIS, Chicago 1997, <http://www.hep.anl.gov/dis97/>;
Proc. of the Int'l Workshop on DIS, Brussels 1998, <http://asrv1.iihe.ac.be/dis98/>.
- [13] A.M. Cooper-Sarkar, R. Devenish & A. De Roeck, Int. J. Mod. Phys. A13 (1998) 3385.
- [14] B.L. Ioffe, Phys. Lett. 40 (1969) 123;
B.L. Ioffe, V.A. Khoze & L.N. Lipatov, *Hard Processes*, North Holland (1984) 185.
- [15] J.J. Sakurai, Ann. Phys. 11 (1960) 1.
- [16] T. Bauer et al., Rev.Mod.Phys. 50 (1978) 261.
- [17] J.J. Sakurai & D. Schildknecht, Phys. Lett. B40 (1972) 121.

- [18] D. Schildknecht & H. Spiesberger, BI-TP 97/25 (1997).
- [19] P. Collins, *An Introduction to Regge Theory and High Energy Physics*, Cambridge University Press 1977.
- [20] E.M. Levin, Lectures on Regge theory, DESY 97-213.
- [21] A. Donnachie & P. Landshoff, Phys. Lett. B296 (1992) 227.
- [22] A. Donnachie & P. Landshoff, Z. Phys. C61 (1994) 139.
- [23] B. Badelek & J. Kwiecinski, Rev. Mod. Phys. 68 (1996) 445.
- [24] A. Levy, Lectures on low x Physics, DESY 97-013.
- [25] H. Spiesberger, K. Charchula & G.A. Schuler , DJANGO6.1.
- [26] K. Kwiatkowski, H. Spiesberger & H.-J. Möhring, Proceedings of the Workshop 'Physics at HERA' vol. 3 DESY (1992) 1294.
- [27] L. Lönnblad, Comp. Phys. Comm. 71 (1992) 15;
L. Lönnblad, Z. Phys. C65 (1995) 285.
- [28] H.-U. Bengtsson & T. Sjöstrand, Comp. Phys. Comm. 46 (1987) 43;
T. Sjöstrand, CERN TH-7112-93 (1994)
- [29] H. Abramowicz et al. , Phys. Lett. B269 (1991) 465.
- [30] B. Badelek, J. Kwiecinski & A. Stasto, Z. Phys. C74 (1997) 297.
- [31] H1 collaboration, I. Abt et al., Nucl. Phys. B497 (1997) 3.
- [32] E665 Collaboration, M.R. Adams et al., Phys.Rev.D54 (1996) 3006.
- [33] D.O. Caldwell et al., Phys.Rev.Lett. 40 (1978) 1222;
S.I. Alekhin et al., CERN-HERA 87-01 (1987).
- [34] ZEUS Collaboration, M. Derrick et al., Z. Phys. C63 (1994) 391;
H1 Collaboration, A. Aid et al., Z. Phys. C69 (1995) 27.
- [35] ZEUS Collaboration, paper No. 792 submitted to ICHEP98 Vancouver, July 1998.
- [36] B. Surov, Ph.D. Thesis, Univ. Hamburg 1998, DESY-THESIS-1998-004;
J.R. Tickner, D.Phil. Thesis, Univ. Oxford 1997, RAL-TH-97-018.
- [37] Regge fits by Donnachie & Landshoff quoted by the Particle Data Group, Phys. Rev. D54 (1996) 191.
- [38] J. Cudell et al., hep-ph/9701312 (1997).
- [39] H. Abramowicz & A. Levy, DESY 97-251.
- [40] H. Navelet, R. Peschanski & S. Wallon, Mod. Phys. Lett A36 (1994) 3393.
- [41] H. Navelet et al., Phys. Lett. B385 (1996) 357.

- [42] H1 Collab., S. Aid et al., Nucl. Phys. B470 (1996) 3.
- [43] K. Prytz, Phys. Lett. B311 (1993) 286; *ibid* B332 (1994) 393.
- [44] J. Bartels, K. Charchula & J. Feltesse, Proceedings of the workshop ‘Physics at HERA’ DESY 1991, Eds W. Buchmüller & G. Ingelman, p193.
- [45] A. Caldwell, Invited talk at the DESY Theory Workshop on ‘Recent Developments in QCD’, October 1997 (unpublished).
- [46] A.D. Martin et al., Eur. Phys. J. C4 (1998) 463.
- [47] NMC, M. Arneodo et al., Nucl. Phys. B483 (1997) 3.
- [48] BCDMS, A.C. Benvenuti et al., Phys. Lett. B223 (1989) 485 & Phys. Lett. B237 (1990) 592.
- [49] H. Georgi & D. Politzer, Phys. Rev. D14 (1976) 1829.
- [50] M. Virchaux & A. Milsztajn, Phys. Lett. B274 (1992) 221.
- [51] A. Bodek & J.L. Ritchie, Phys. Rev. D23 (1981) 1070.
- [52] G. Gurci, W. Furmanski & R. Petronzio, Nucl. Phys. B175 (1980) 27; W. Furmanski & R. Petronzio, Phys. Lett. 97B (1980) 437 & Z. Phys. C11 (1982) 293.
- [53] S. Riemersma et al., Phys. Lett. B347 (1995) 143 and references therein.
- [54] A.D. Martin, R.G. Roberts & W.J. Stirling, Phys. Lett. B387 (1996) 419.
- [55] Particle Data Group, R.M. Barnett et al., Phys. Rev. D54 (1996) 1.
- [56] M. Botje, QCDNUM version 16.11 (unpublished).
- [57] F. James, Minuit Version 94.1, CERN Program Library Long Writeup D506.
- [58] ZEUS Collaboration, J. Breitweg et al., Phys. Lett. B407 (1997) 402.
- [59] C. Pascaud & F. Zomer, preprint LAL 95-05.
- [60] M. Abramowitz & I.A. Stegun, *Handbook of Mathematical Functions*, Dover Publications, Inc. (1972).
- [61] W.J. Stirling, private communication.
- [62] G. Altarelli & G. Martinelli, Phys. Lett. B76 (1978) 89.
- [63] C. Lopez, F. Barreiro & F.J. Yndurain, Z. Phys. C72 (1996) 561; F. Barreiro, Proc. ICHEP96 Warsaw, eds Z. Ajduk & A.K. Wroblewski, World Sci. (1997) p653.
- [64] M. Glück, E. Reya & A. Vogt, hep-ph/9806404.

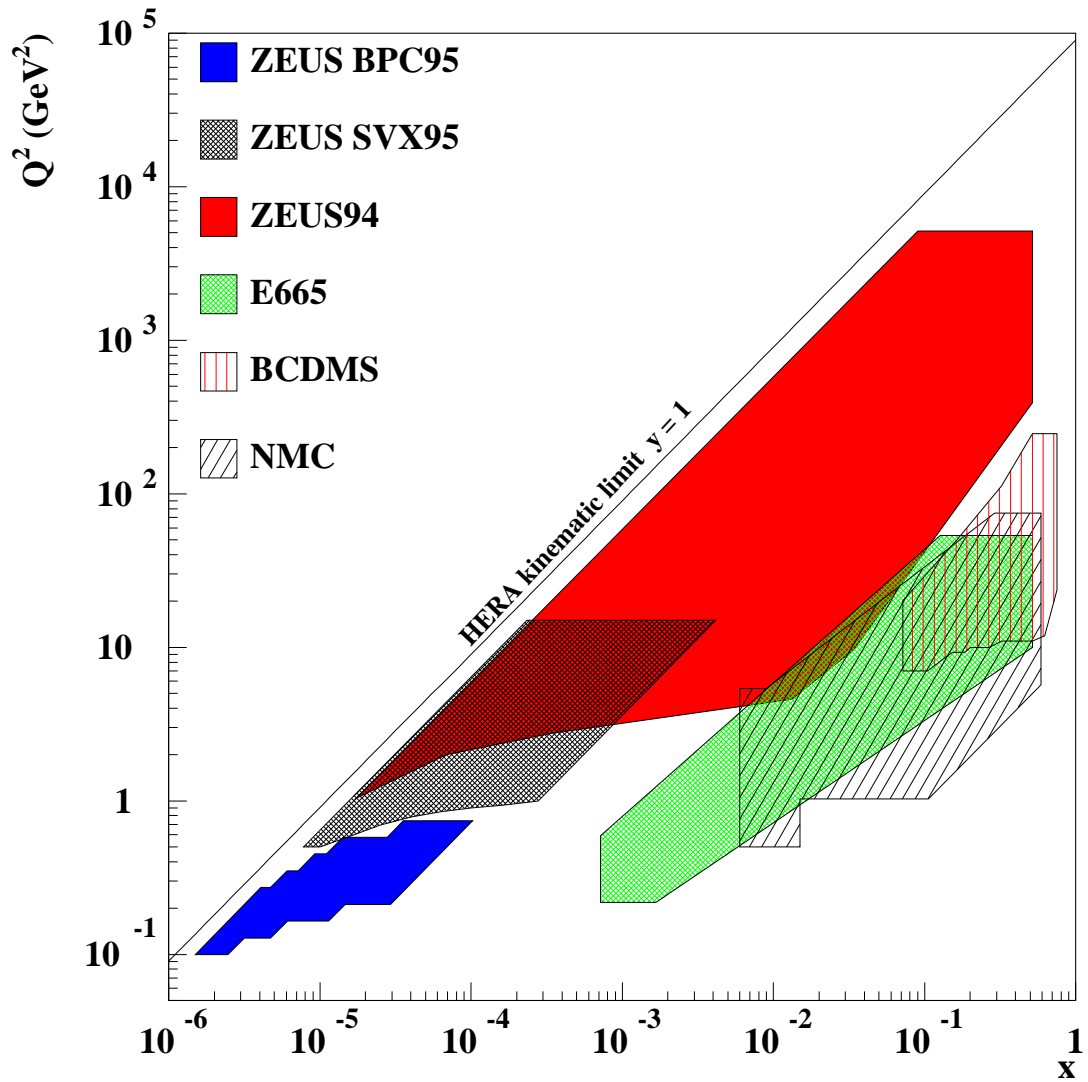


Figure 1: The (x, Q^2) plane showing the regions covered by the ZEUS data sets BPC95, ZEUS94 and SVX95 together with regions covered by the fixed target experiments E665, BCDMS and NMC.

ZEUS 1995

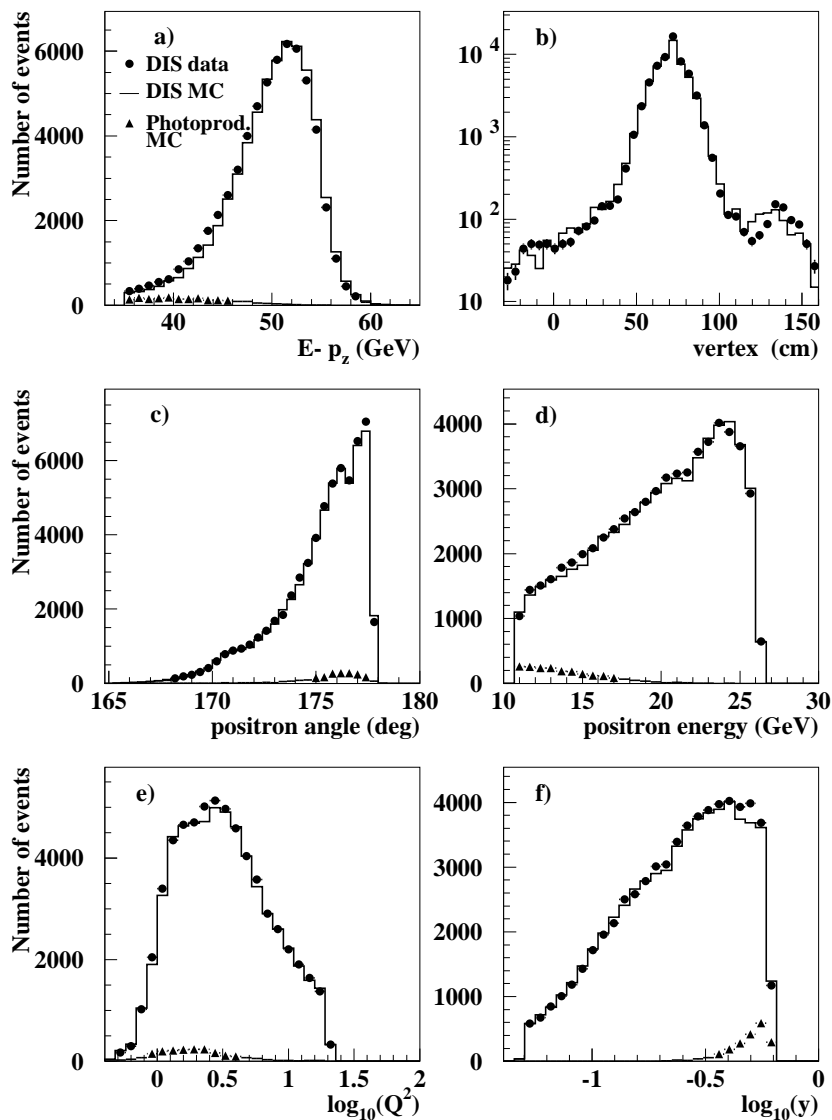


Figure 2: Distributions from the SVX95 analysis showing the comparison between data and simulation: (a) δ or $E - P_Z$ as defined in Sec. 3.3; (b) the Z -position of the primary vertex; (c) the positron scattering angle θ_e ; (d) the energy, E'_e , of the scattered positron; (e) $\log_{10} Q^2$; (f) $\log_{10} y$. In all cases the data are represented by filled circles, the simulation by the open histograms and the photoproduction background (calculated from the MC described in Sec. 3.1) by the filled triangles. Both MC calculations are normalised to the luminosity of the data.

ZEUS 1995

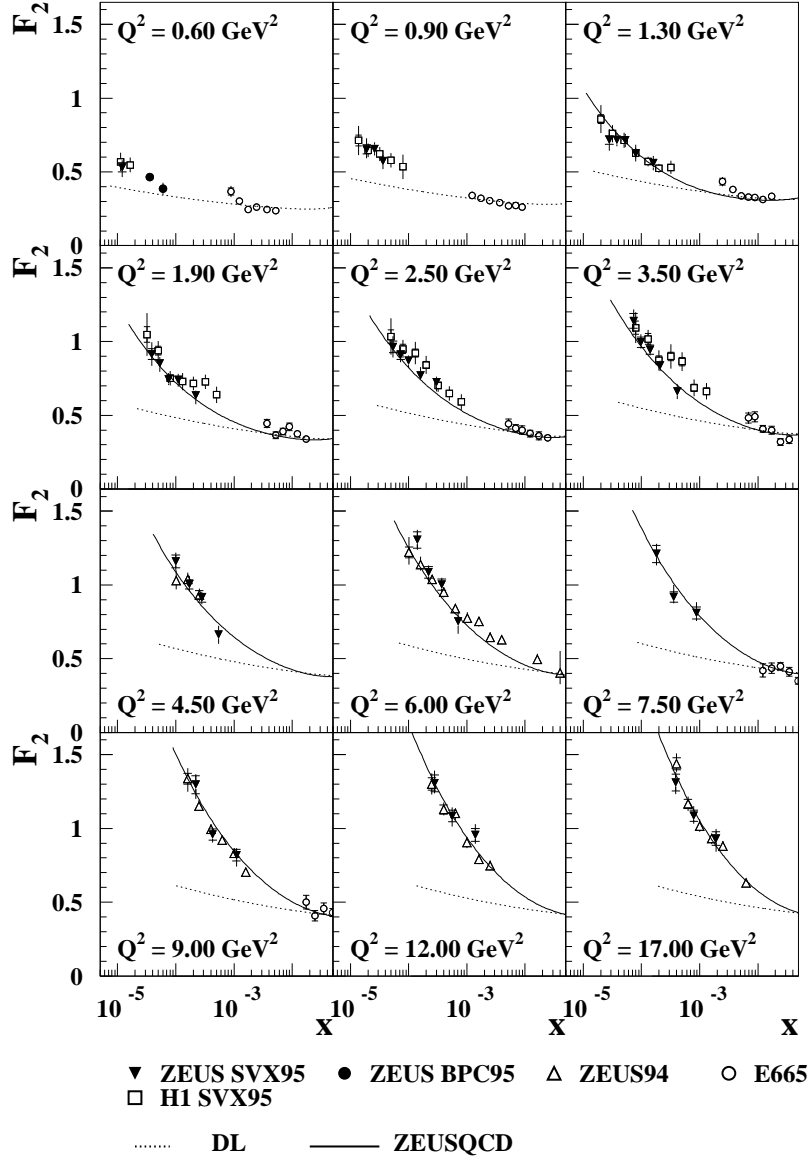


Figure 3: The ZEUS SVX95 F_2 data as a function of x for different Q^2 bins together with previous ZEUS data (ZEUS 1994 [4], ZEUS BPC 1995 [2]), data from H1 SVX95 [31] and fixed target data (E665 [32]). Error bars correspond to the statistical and systematic errors added in quadrature. The overall normalisation errors are not shown. The curves shown are (dotted) the Donnachie-Landshoff Regge model [22] and (full) the ZEUS NLO QCD fit.

ZEUS 1995

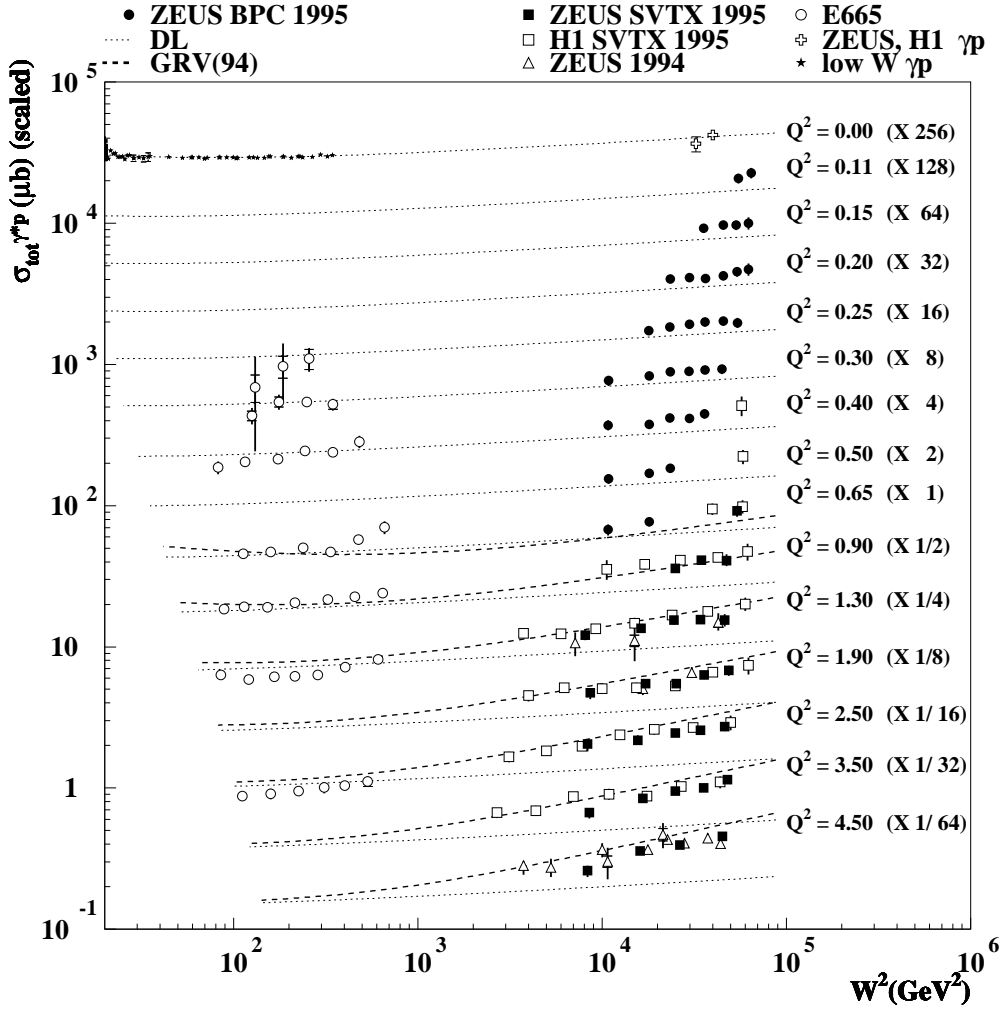


Figure 4: The total $\gamma^* p$ cross-section, $\sigma_{\text{tot}}^{\gamma^* p}$, as a function of W^2 at different Q^2 [GeV²]. The data of this analysis (ZEUS SVX95) are shown together with previous ZEUS and H1 data (ZEUS94, ZEUS BPC95, H1 SVX95). Also the total photoproduction cross-sections from ZEUS and H1 and from fixed target experiments at lower W are shown. Predictions from the DL [22] and GRV94 [8] models are indicated by the dotted and dashed curves, respectively.

ZEUS 1995

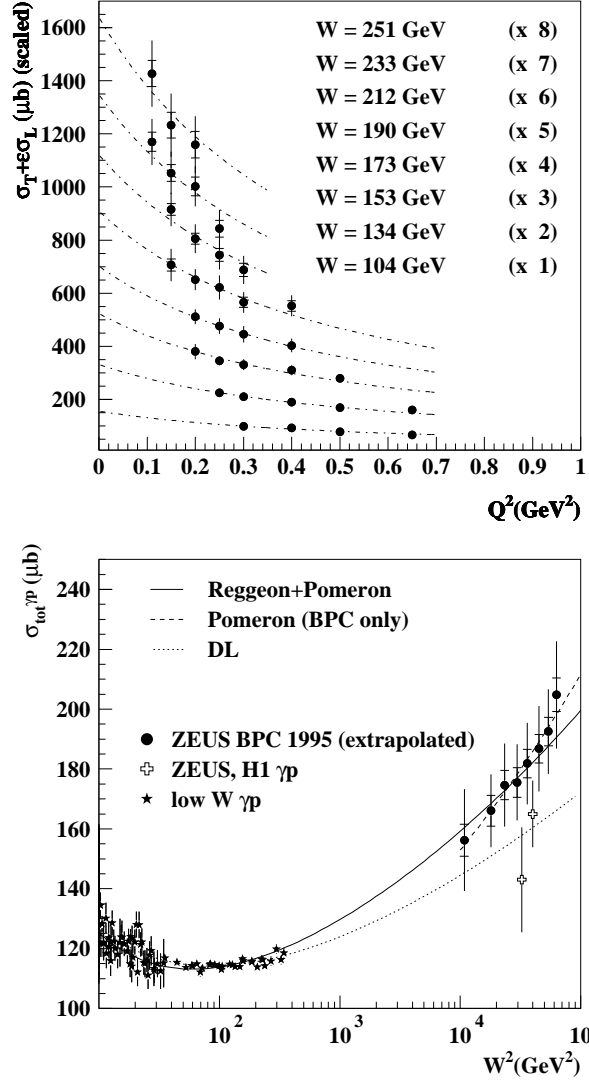


Figure 5: *Upper plot.* ZEUS BPC measurements of the total cross-section $\sigma_T + \epsilon\sigma_L$ in bins of W as a function of Q^2 and the GVMD fit to the data. *Lower plot.* $\sigma_{\text{tot}}^{\gamma p}$ as a function of W^2 . The ZEUS BPC95 points are those from the GVMD extrapolation ($\sigma_0^{\gamma p}$). Also shown are direct measurements of the total photoproduction cross-section from H1, ZEUS and earlier experiments at low energies. The curves show Regge fits: the original DL fit [22] to the low W data (dotted); the Pomeron only fit to the BPC $\sigma_0^{\gamma p}$ data (dashed) and the Pomeron+Reggeon fit to the low W and BPC $\sigma_0^{\gamma p}$ data (full).

ZEUS 1995

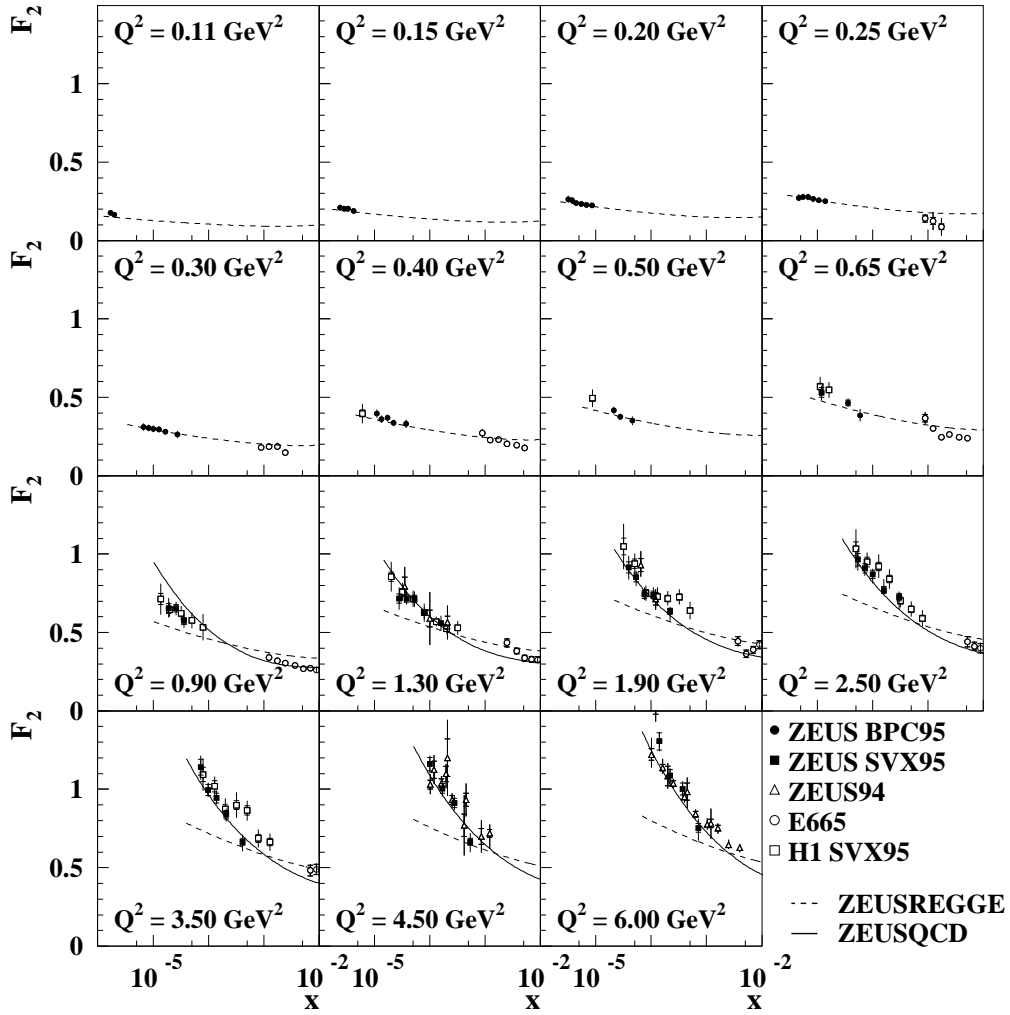


Figure 6: Low Q^2 F_2 data for different Q^2 bins together with the ZEUS Regge fit (dashed curves) to the BPC95 data as described in Sec. 4. Also shown at larger values of Q^2 is the ZEUS NLO QCD fit (full curves) as described in Sec. 6.

ZEUS 1995

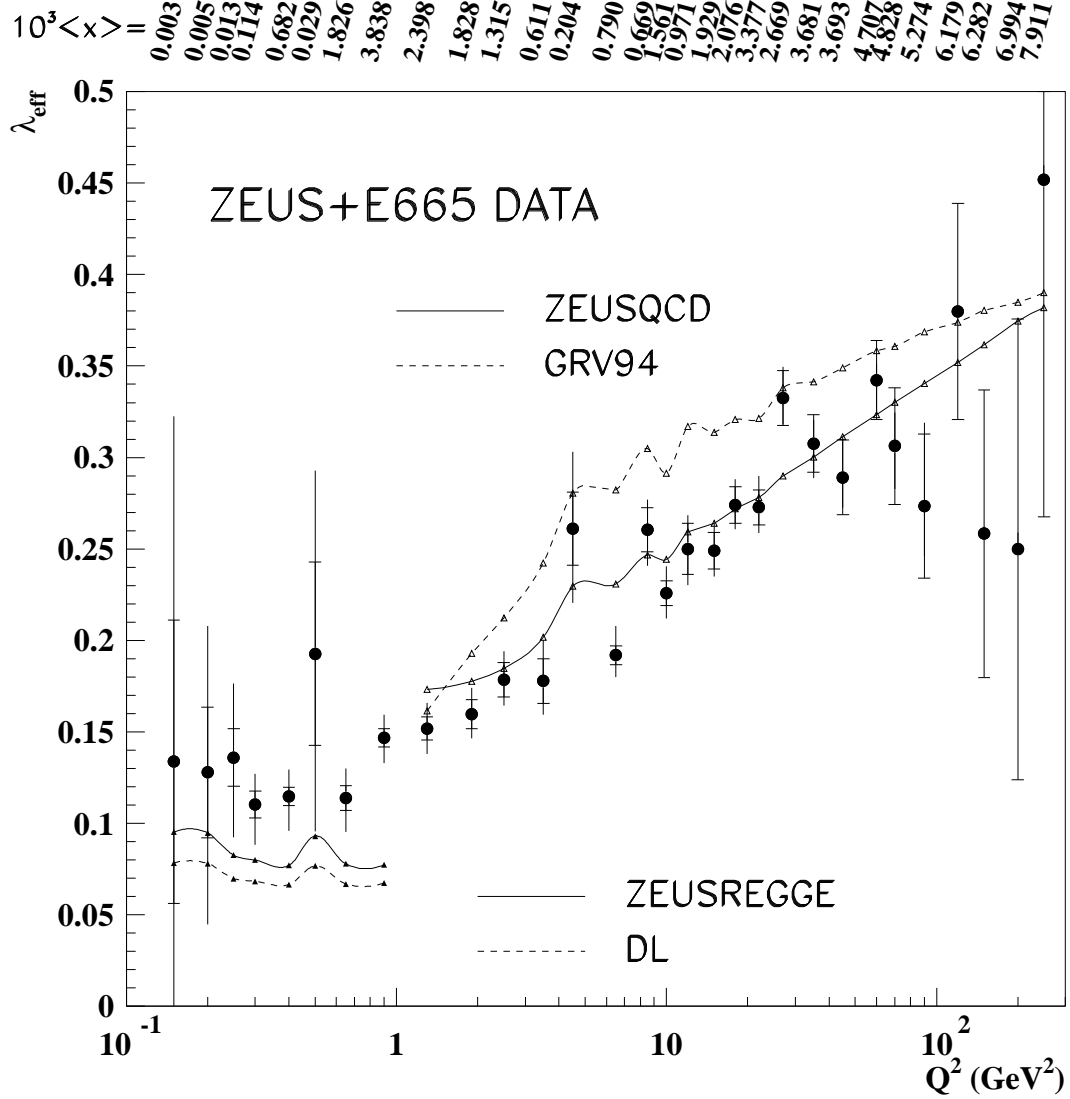


Figure 7: $\lambda_{eff} = d \ln F_2 / d \ln(1/x)$ as a function of Q^2 calculated by fitting $F_2 = Ax^{-\lambda_{eff}}$ to ZEUS and E665 data with $x < 0.01$. The inner error bar shows the statistical error and the outer the total statistical and systematic error added in quadrature. $\langle x \rangle$ is calculated as described in Sec. 5.1. The DL and GRV94 calculations, shown as points linked by dashed lines, are from the Donnachie-Landshoff Regge fit [22] and the GRV94 NLO QCD fit [8], respectively. The ZEUSREGGE and ZEUSQCD calculations, shown as points linked by full lines, are from the ZEUS Regge and NLO QCD fits described in Secs 4 and 6 of the text respectively. In all cases the points are obtained using the same weighted range of x as for the experimental data.

ZEUS 1995

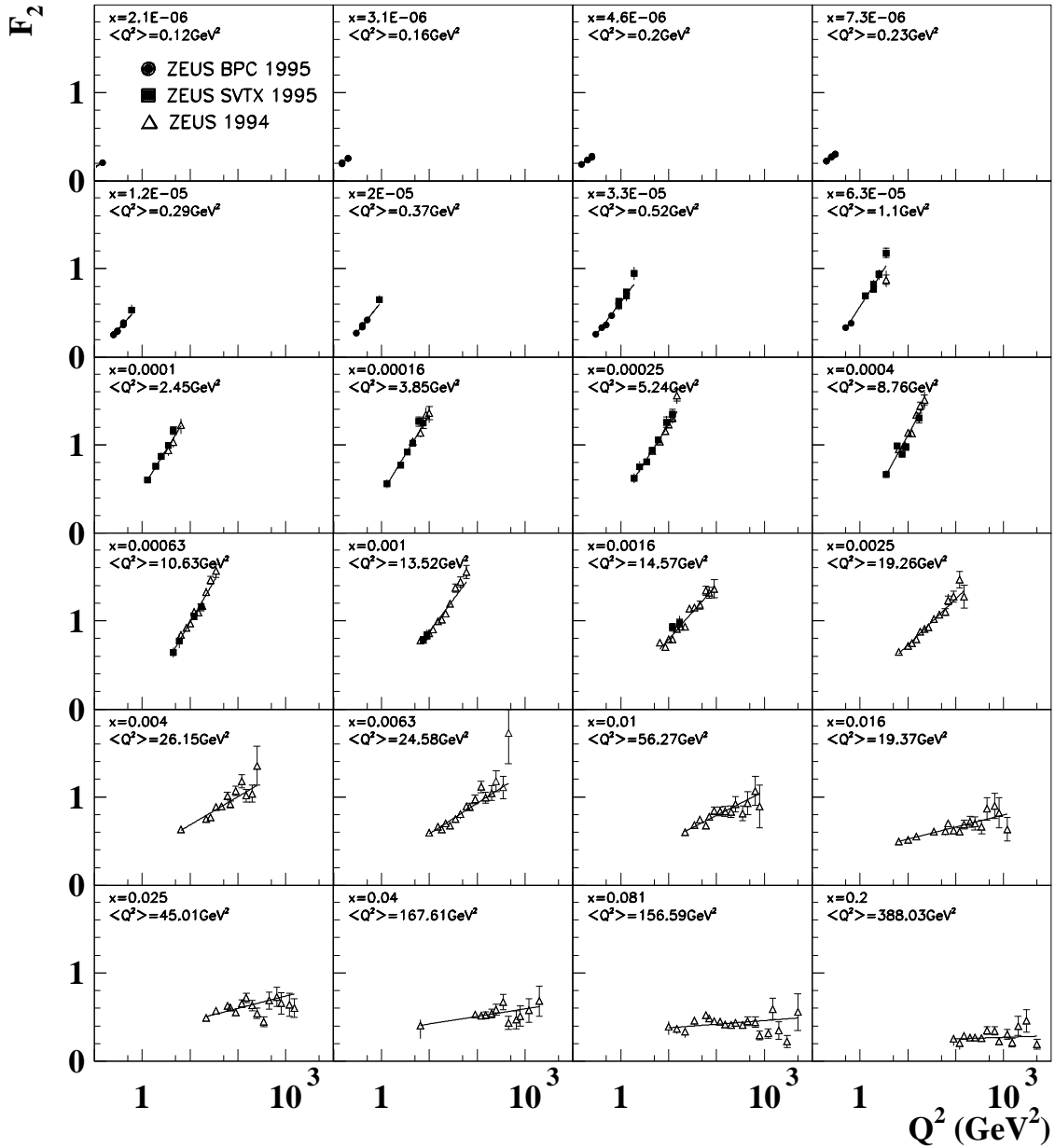


Figure 8: F_2 as a function of Q^2 in bins of x from the ZEUS data sets BPC95, SVX95, ZEUS94. The linear fits $F_2 = a + b \ln Q^2$ are also shown. The values of $\langle Q^2 \rangle$ given in the plots are calculated as described in Sec. 5.2.

ZEUS 1995

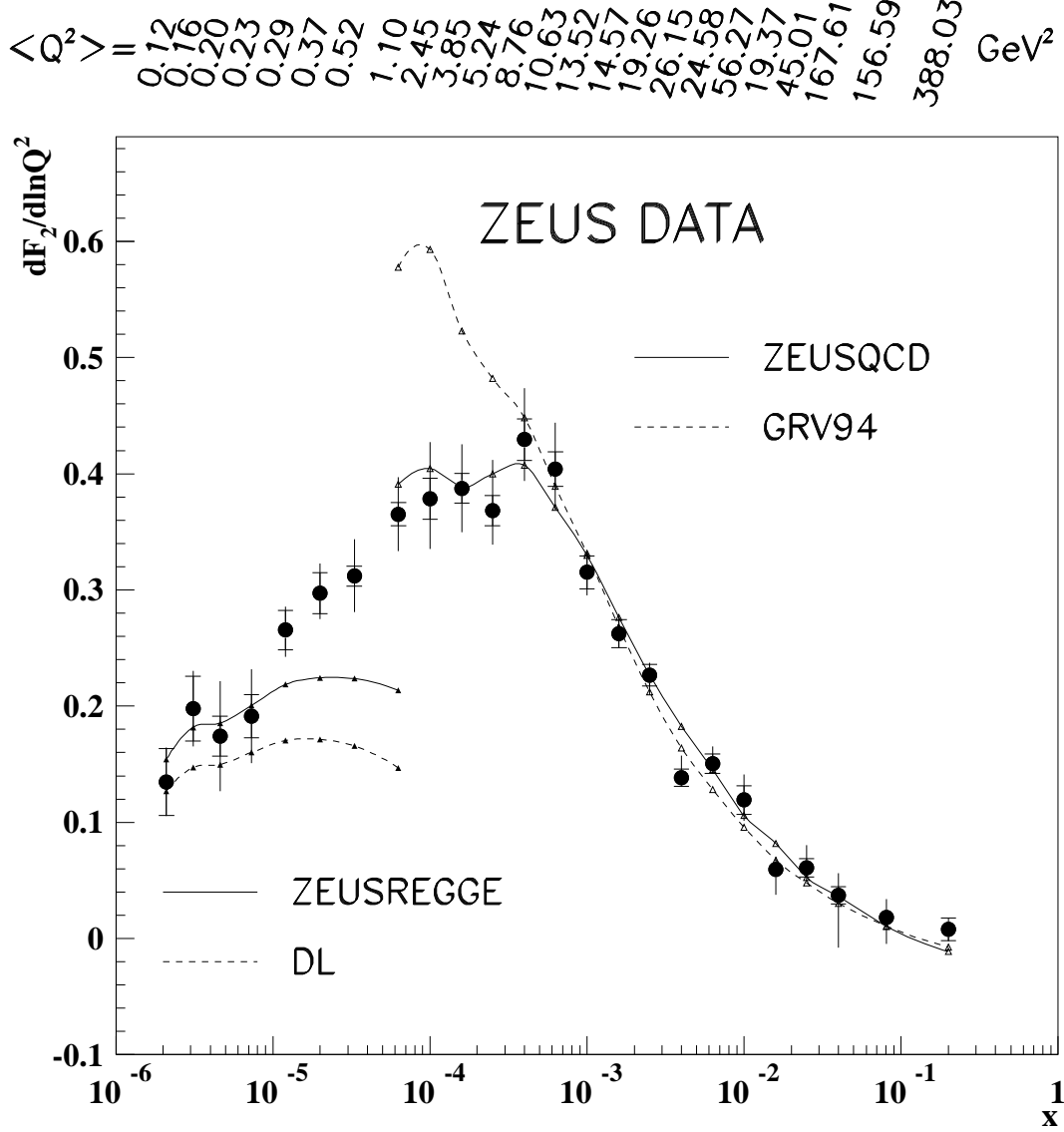


Figure 9: $dF_2/d\ln Q^2$ as a function of x calculated by fitting ZEUS F_2 data in bins of x to the form $a + b \ln Q^2$. The inner error bar shows the statistical error and the outer the total statistical and systematic error added in quadrature. $\langle Q^2 \rangle$ is calculated as described in Sec. 5.2. The DL and GRV94 calculations, shown as points linked by dashed lines, are from the Donnachie-Landshoff Regge fit [22] and the GRV94 NLO QCD fit [8], respectively. The ZEUSREGGE and ZEUSQCD calculations, shown as points linked by full lines, are from the ZEUS Regge and NLO QCD fits described in Secs 4 and 6 of the text respectively. In all cases the points are obtained using the same weighted range of Q^2 as for the experimental data.

$F_2 + C_i$

ZEUS 1995

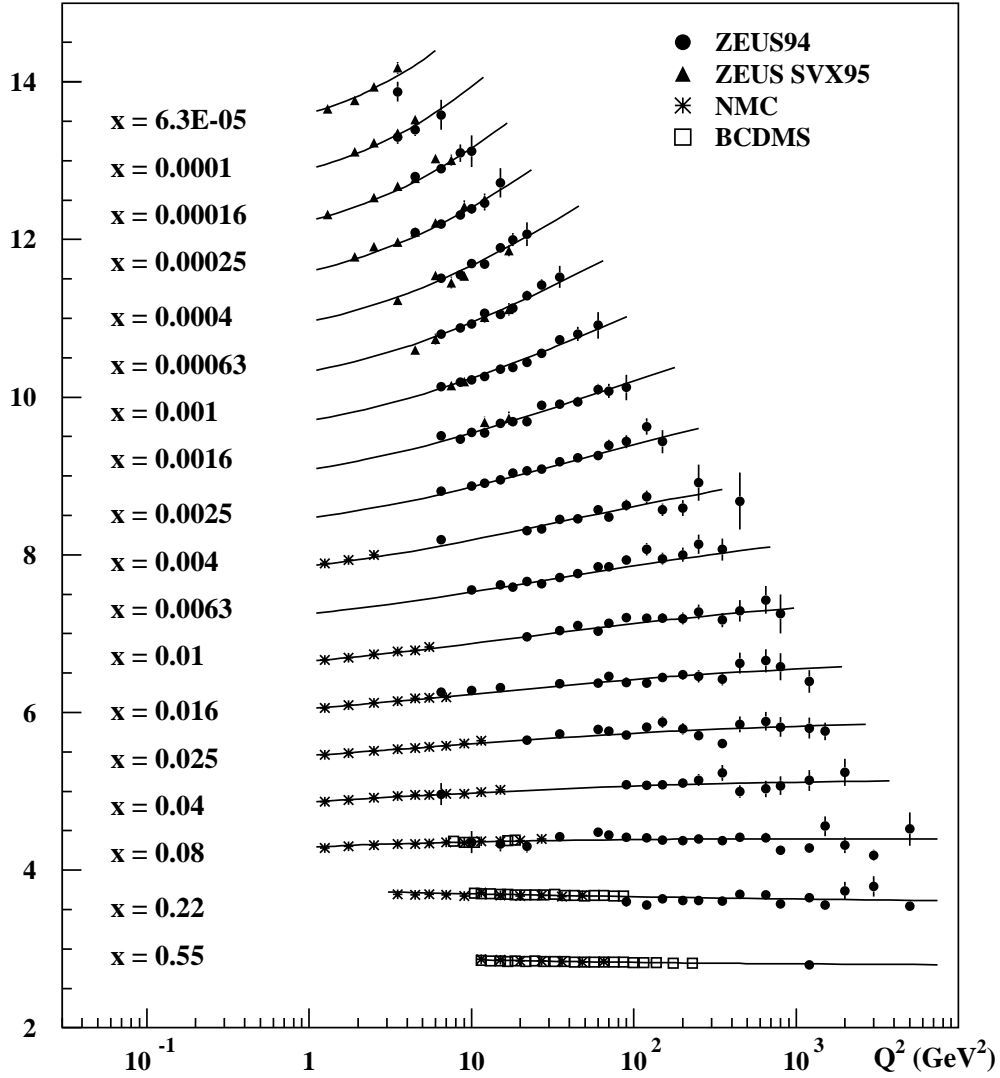


Figure 10: The proton structure function F_2 versus Q^2 at fixed values of x . Data are from the ZEUS94 and SVX95 analyses and from the NMC and BCDMS fixed target experiments. The solid lines correspond to the QCD fit described in the text. For clarity an amount $C_i = 13.6 - 0.6i$ is added to F_2 where $i = 1$ (18) for the lowest (highest) x value.

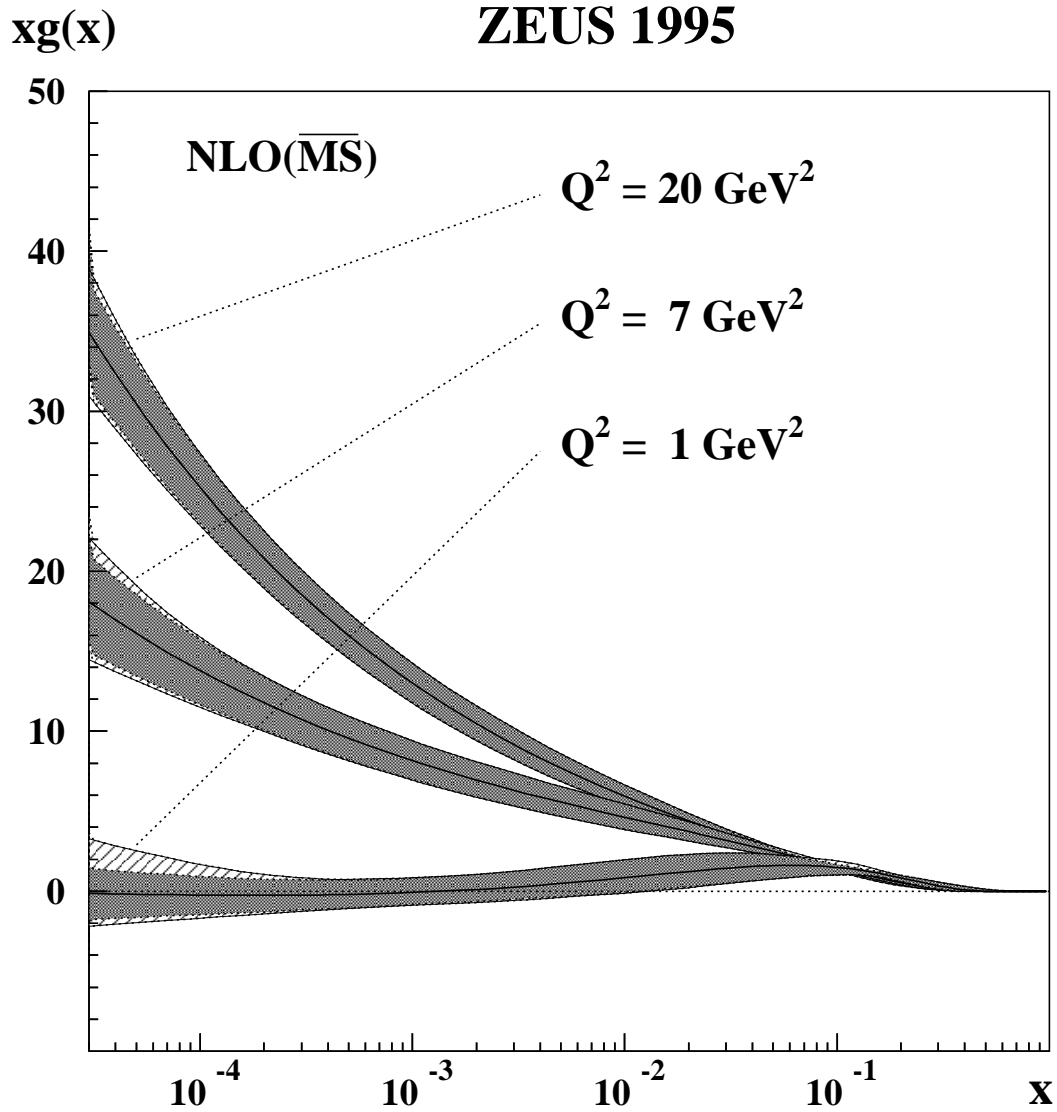


Figure 11: The gluon momentum distribution $xg(x)$ as a function of x at fixed values of $Q^2 = 1, 7$ and 20 GeV^2 from the ZEUS QCD fit. The inner shaded bands show the ‘HERA standard’ errors of Sec. 6. The outer hatched bands indicate the quadratic sum of the ‘HERA standard’ and the ‘parameterisation’ errors.

ZEUS 1995

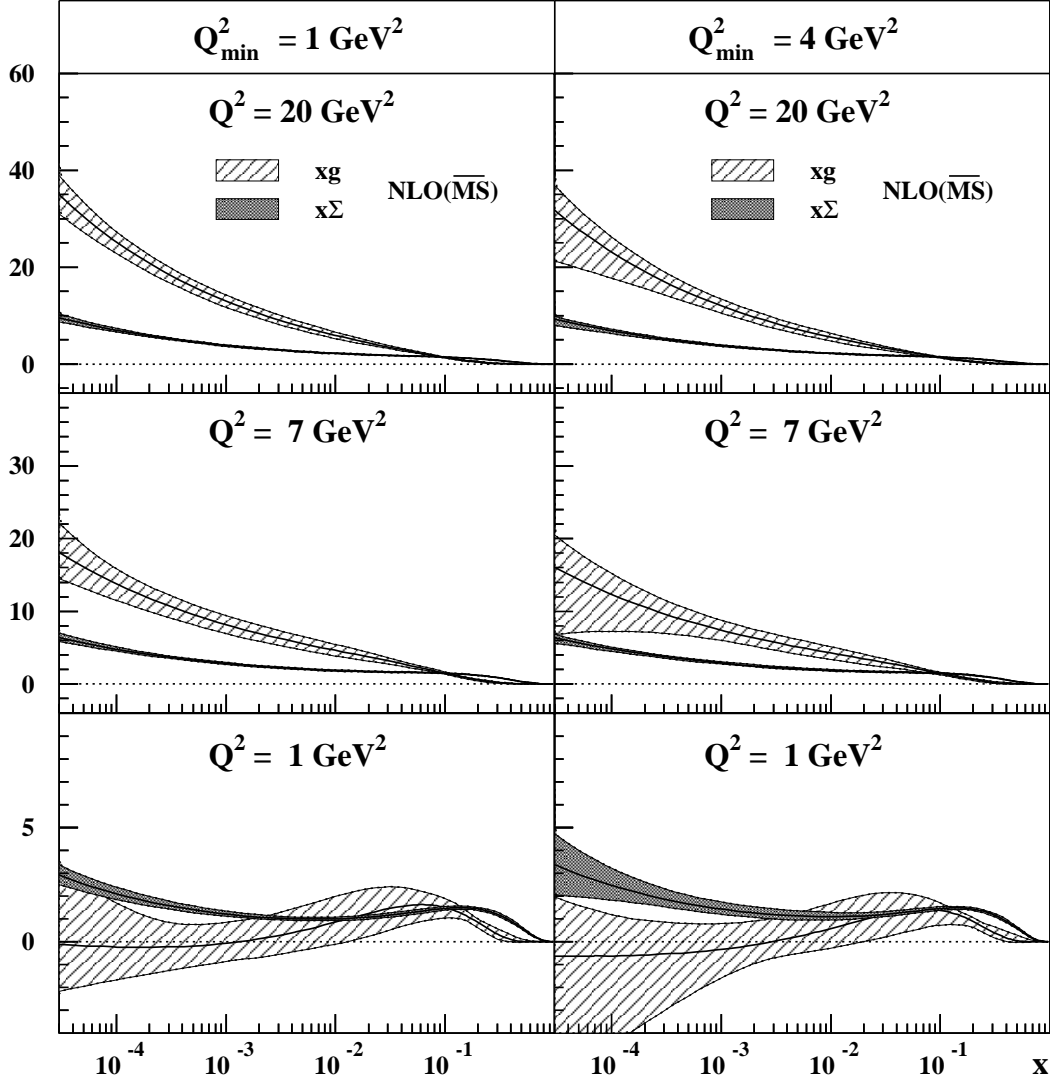


Figure 12: The quark singlet momentum distribution, $x\Sigma$ (shaded), and the gluon momentum distribution, $xg(x)$ (hatched), as functions of x at fixed values of $Q^2 = 1, 7$ and 20 GeV^2 from the ZEUS QCD fit. The error bands correspond to the quadratic sum of all error sources considered for each parton density. The three left-hand plots show the results from the standard fit of Sec. 6 including F_2 data with $Q^2 > 1 \text{ GeV}^2$; the three right-hand plots show the corresponding results from the fit described in Sec. 7 for which the data must satisfy $Q^2 > 4 \text{ GeV}^2$.